# Motion Planning Strategies for Safety Procedure of Multi-Satellite Formation Flying Systems\*

Francesca Scala†

Microwaves and Radar Institute, German Aerospace Center DLR, Münchener Straße 20, 82234 Weßling, Germany

Mateus Silva Borges‡

Technological Institute of Aeronautics (ITA), São José dos Campos - SP, 12228-900, Brazil

Michelangelo Villano§

Microwaves and Radar Institute, German Aerospace Center DLR, Münchener Straße 20, 82234 Weßling, Germany

The concept of multiple satellites in formation brings a significant advancement in enhancing the performance of single-pass synthetic aperture radar interferometry. Maintaining a constant baseline is vital to enhance interferometric acquisition and poses significant challenges to the safety conditions of the vehicles. This study presents a motion planning strategy specifically designed to address safety procedures in case of anomalous onboard conditions for a fast reconfiguration to the safe mode. The research examines two approaches: the linear quadratic regulator (LQR) and the model predictive control (MPC). It investigates the capability of different controllers for fast formation reconfiguration in terms of minimum propellant consumption and passive safety. We demonstrate that the MPC controller can autonomously plan and implement an optimal maneuver in less than one orbital period. On the other hand, the LQR can benefit from an automatic tuning of the gains to track an optimal reference trajectory. As a practical implication, this research provides solutions to maintaining a safe formation with constant baselines, proposing different control schemes.

#### **Nomenclature**

N	(-)	=	Number of satellites
$[\cdot]_j$	(-)	=	Index for the number of satellite $j = 1,, N$
t	(seconds)	=	Time variable
K	(-)	=	Number of discretized time steps
k	(-)	=	Index for the discretized time step $k = 1,, K$

<sup>\*</sup>Part of the work presented in this manuscript was presented with the paper no. AAS 24-385 at the 2024 AAS/AIAA Astrodynamics Specialist Conference, August 11-15, Broomfield, CO.

<sup>†</sup>Post-Doctoral Researcher, Microwaves and Radar Institute, francesca1.scala@polimi.it. (currently at OHB System) (Corresponding Author)

<sup>&</sup>lt;sup>‡</sup>BSc Student, Technological Institue of Aeronautics, mateus.borges@ga.ita.br.

<sup>§</sup>Head of the NewSpace SAR Research Group, Microwaves and Radar Institute, michelangelo.villano@dlr.de.

$\Delta t$	(seconds)	=	Discretized time step
a	(m)	=	Semi-major axis
λ	(deg)	=	Mean argument of latitude
$e_x, e_y$	(-,-)	=	Components of the eccentricity vector
i	(deg)	=	Inclination
Ω	(deg)	=	Right ascension of the ascending node
$\omega$	(deg)	=	Argument of perigee
M	(deg)	=	Mean anomaly
$\theta$	(deg)	=	True anomaly
n	(1/seconds)	=	Mean motion of the orbit
$\delta a$	(-)	=	Relative semi-major axis
$\delta\lambda$	(-)	=	Relative mean argument of latitude
$\delta e_x, \delta e_y$	(-,-)	=	Components of the relative eccentricity vector
$\delta i_x, \delta i_y$	(-,-)	=	Components of the relative inclination vector
u	(m/s)	=	Vector of the relative control input
$\hat{\mathbf{X}}$	(m)	=	Decision vector for the sequential convex optimization
$\hat{\mathbf{J}}$	(m/s)	=	Cost function for the sequential convex optimization
$[\cdot]_0$	(-)	=	Initial conditions
$[\cdot]_f$	(-)	=	Final conditions
$\mathbf{J}_{lqr}$	(m/s)	=	Cost function for the LQR optimization
$\mathbf{Q}, \mathbf{R}$	$(1/m^2)$ , (seconds <sup>4</sup> /m <sup>2</sup> )	=	Weight matrices for the state error and the control variable of the LQR
$\epsilon$	(m)	=	Threshold for the integral time absolute error
$T_f$	(seconds)	=	Maneuver time
$d_{coll}$	(m)	=	Minimum inter-satellite collision distance
$m_{sc}$	(kg)	=	Spacecraft mass

# I. Introduction

The concept of relative motion and formation flying has gained importance in Earth observation and remote sensing missions. Specifically, for interferometric synthetic aperture radar (InSAR) applications, the idea of flying multiple satellites cooperating to improve scientific outcomes is appealing for several reasons, as demonstrated by multiple studies [1–4]. First, it allows for reducing the complexity of individual satellites and, simultaneously, a higher robustness against failure than a single platform. For example, in case of a malfunction of one of the platforms, replacing a new satellite

does not jeopardize the entire mission, as would happen for the single satellite case. Similarly, formation flying systems are flexible for future expansion with additional satellites that can enhance interferometric performance or support different operational modes. As an example, the TanDEM-X mission exemplified the effectiveness of formation flying systems for single-pass InSAR, enabling the generation of high-resolution digital elevation models (DEMs), thanks to the precise control of the interferometric baselines, which slowly vary in hundreds of meters range [5–7]. Another example is the MirrorSAR concept, where three small receive-only satellites were conceived for the High-Resolution Wide-Swath (HRWS) mission to provide continuity in the X-band data and allow for the generation of a DEM more accurate than TanDEM-X through the exploitation of multiple baselines [8]. A different approach was proposed in [9, 10], where constant separation between the satellites is envisioned. The proposed configuration consists of two or more satellites flying in parallel tracks, with a constant separation in the out-of-plane direction. The concept of fixed baseline has the potential to enhance novel InSAR mission concepts, as it enables the constant performance of a DEM to be achieved. Differently from the helix configuration, which guarantees passive safety during the flight [11–13], maintaining parallel tracks among the platforms introduces new challenges from the safety and risk point of view. In the fixed-baseline scenario, the onboard controller must correct the drift due to the external orbital perturbations and the natural harmonic oscillations of the dynamics in the out-of-plane direction. This increases the fuel consumption compared with the helix solution [9, 10], and requires a specific motion planning strategy for safe mode reconfiguration to ensure safety throughout the mission [9]. The safety of the formation flying systems has been investigated due to their importance in enabling safe operation, especially when meter-to-kilometer distances are involved [11-13]. However, these studies focus on the design of passive safety configurations based on helix relative trajectories, and they cannot be directly applied to the fixed-baseline scenarios in [9, 10].

Nowadays, autonomous strategies for safety operations must be developed to support the feasibility of future mission designs based on fixed baselines. This manuscript addresses the need for strategies for safety operations when fixed baselines are considered for interferometric acquisition. Because of the continuous nature of the control for drift compensation to keep the constant baseline, we investigate the possibility of implementing low thrust control not only for formation maintenance purposes, as in [14–17], but also for developing a motion planning strategy to enter the safe mode. In the following, we have implemented a strategy under multiple control algorithms in a closed-loop system to understand the performance and the advantages of one controller compared to another in terms of minimum delta-velocity consumption, responsiveness of the control, and control accuracy. As a starting condition, we consider the case of a system of 3 or more satellites flying in parallel tracks. In contrast, the target condition for the safe mode is a passive safety configuration, such as the helix trajectory. In the analysis, we investigate three control strategies in closed loop to design the maneuver: (i) the model predictive controller (MPC), (ii) the linear quadratic regulator (LQR) controller, (iii) a novel automatically adaptive linear quadratic regulator (aLQR) controller. The classic and the adaptive LQR feedback controllers implement a commanded control based on the error between the current and desired states

[18, 19]. The LOR approach has been widely used to correct imperfections of maneuvers in the presence of external perturbations. Its implementation is based on the selection of weight matrices to compute the optimal control gain, often based on a trial-and-error method, until the solution meets the simulation requirements [20, 21]. Few studies proposed heuristic methodologies to compute the control gain for the optimization of the problem [22, 23], and most of these works present suggestions for LQR gain selections for specific geometries or scenarios. Starting from these considerations, in the manuscript, we first implement the classic version of the LQR, and then we propose a novel approach to tune the control gains optimally with an aLQR. On the other hand, the MPC is based on the feedback of the current state into a trajectory optimization to correct and optimize the subsequent control actions accordingly. In recent years, multiple solutions based on MPC have been provided in literature studies, demonstrating the advantages and disadvantages of the methodology [24]. Specifically, MPC offers robustness to disturbances and the ability to handle constraints in the algorithm's formulation. Thanks to the mathematical representation in the convex formulation, sub-optimal solutions in terms of control profile are ensured. The fuel-optimal MPC formulation was proposed in the literature to address onboard implementation with collision avoidance constraints [25]. Later, convex trajectory optimization methodologies were studied for a swarm of satellites in combination with Earth's oblateness  $J_2$  invariant orbits and collision avoidance constraints [26, 27]. These studies open the investigation for different applications with formation flying, explicitly addressing the need for autonomous task assignment and autonomous reconfiguration procedures in orbit [14, 15]. Recent studies couple the representation of the Relative Orbital Elements (ROE) dynamics together with optimal guidance solutions and MPC. A maneuver planning algorithm for satellite formations using mean relative orbital elements was proposed for a distributed system of satellites to assess the fuel consumption performances [16]. In contrast, the relative and absolute orbit control in a high-drag environment was investigated in [17, 18]. Additionally, these recent works include collision avoidance constraints among the satellites in the distributed system to ensure safety during orbit operations. Starting from these outcomes, we developed a maneuver planning algorithm in combination with MPC, incorporating the main external perturbations in the LEO region to accurately represent the orbital environment, such as the Earth's oblateness  $(J_2)$  and the atmospheric drag. Unlike previous studies, we specifically tailor the control technique for formation reconfiguration scenarios when short satellite distances are involved (< 100 m) and parallel relative orbit tracks are considered for fixed-baseline configurations. Consequently, a reconfiguration in less than one orbital period is planned to ensure a fast transition to safe mode.

The manuscript provides three main contributions to the current state of the art: (i) investigation and performance comparison of multiple evolutionary algorithms for optimal control gains for the aLQR controller, (ii) low thrust MPC maneuver planning for fast transition to safe mode in combination with convex optimization, (iii) control accuracy and delta-velocity assessment during a reconfiguration maneuver from interferometric SAR acquisition mode to safe mode for the case of a fixed-baseline formation. Specifically, Section II of the paper describes the problem setup and the dynamical model implemented in the control. Section III provides a detailed description of the control methodologies

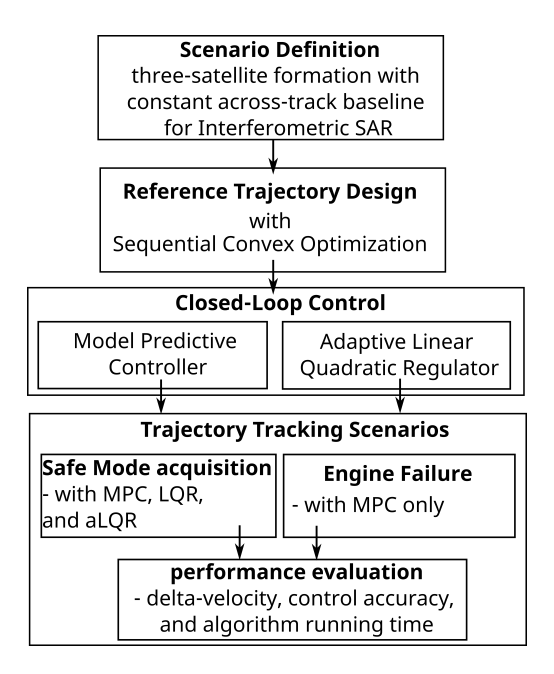


Fig. 1 Flow diagram of the manuscript content.

implemented in the simulation and their algorithm representations. Finally, Sections IV and V illustrate the results for the scenarios under analysis and the final considerations, respectively. A flow diagram of the manuscript content is shown in Figure 1, to clarify the approach better for the analyses.

# **II. Problem Settings**

Starting from the analyses presented in [9, 10], we consider a formation of three spacecraft in a fixed-baseline configuration to perform single-pass across-track SAR interferometry. The satellites are kept with a constant separation in the across-track direction to maintain the relative trajectories parallel to each other during the SAR acquisition phase. As demonstrated in [9], this configuration is promising, in combination with small baselines (< 100 m), to reduce propellant consumption for formation maintenance. For this reason, one possible application of this configuration envisions a formation of satellites with radar operating in the Ka-band of the electromagnetic spectrum, where relatively short baselines would still allow for accurate DEM generation [4]. As the introduction outlines, a robust safety procedure is essential when continuously controlling spacecraft flying at short distances. As demonstrated in [28], in the case of fault or anomaly conditions, such as an onboard failure and potential recovery after a fault, the controller should plan a reconfiguration maneuver to a safe mode, ensuring passive safety in the shortest time possible. Following the analyses in [28], we implement an optimal trajectory design for the reconfiguration maneuver from the nominal SAR observation configuration to the safe mode. Under a continuous control scheme, the initial configuration consists of spacecraft flying in parallel tracks, as in Fig. 2 (left). The latter uses the helix configuration to implement the passive safety condition, as shown in Fig. 2 (right).

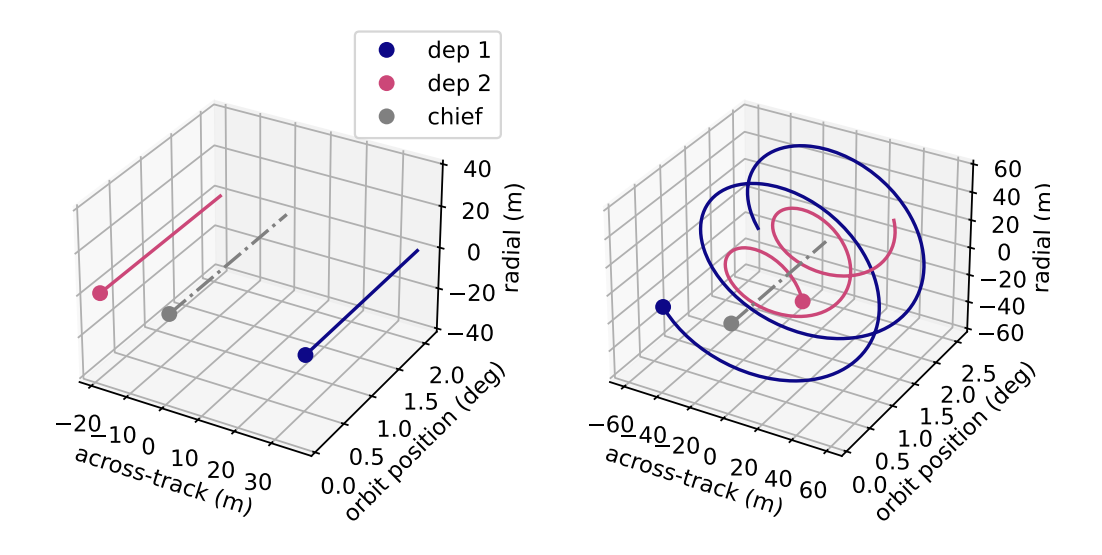


Fig. 2 Three satellites flying in a fixed-baseline configuration (left) and in a nested helix configuration (right).

The optimal reconfiguration trajectory is based on a convex optimization procedure, and it aims at minimizing the propellant consumption for the maneuver, considering multiple constraints: a maximum thrust level, a minimum distance among the satellites for safety purposes, and a limitation on the maneuver time. To assess the feasibility of the reconfiguration, we implement a closed-loop MPC control algorithm, starting from the analyses in [28], and two different closed-loop control schemes based on the classic LQR controller and an aLQR, based on evolutionary algorithms for optimal control gains. In the following sections, we introduce the dynamical model adopted in the controllers.

#### A. Relative Dynamical Model

The relative motion of multiple satellites flying in formation is described with quasi-non-singular ROE, as introduced in [29]. We describe the relative motion considering one primary (or chief) satellite and multiple secondary (or deputies) satellites flying around the main one. For a formation of N satellites, we introduce the index j to describe the parameters of the j-th secondary satellite, with j = 1, ..., N. The absolute orbit of the main satellite is identified by non-singular Keplerian elements, also known as Ustinov elements,  $el_c = \{a, \lambda, e_x, e_y, i, \Omega\}_c$  [30]. Similarly, the non-singular Keplerian elements of the j-th secondary satellite are  $el_j = \{a, \lambda, e_x, e_y, i, \Omega\}_j$ . The quantity a is the orbit semi-major axis,  $\lambda = \omega + M$  is the mean argument of latitude depending on the argument of perigee  $\omega$  and mean anomaly M,  $\{e_x, e_y\}$  are the x and y components of the eccentricity vector, e cos  $\omega$  and e sin  $\omega$ , respectively, i is the orbit inclination, and  $\Omega$  is the right ascension of the ascending node. In the present manuscript, the mean orbital elements are used instead of the osculating elements for the analyses with the feedback control based on relative orbital elements (ROE). The mean-to-osculating transformation was computed based on Hamiltonian perturbation theory by Lie transforms, as derived in [31]. The advantage of this analytical formulation lies in the time efficiency of the computation and the

possibility of coping with equatorial and circular orbits without introducing singularities. An alternative formulation for the osculating-to-mean elements was proposed in [30], where the mean elements are obtained in an iterative way, where the correction was applied using the Eckstein-Ustinov theory. From this representation, the quasi-non-singular ROEs are defined in Eq. 1, where  $\delta a_j$  is the relative semi-major axis,  $\delta \lambda_j$  is the relative mean argument of latitude,  $\delta e_{x_j}$  and  $\delta e_{y_j}$  are the x and y components of the relative eccentricity vector  $\delta e_j$ , whereas  $\delta i_{x_j}$  and  $\delta i_{y_j}$  are the x and y components of the relative inclination vector  $\delta i_j$  [29].

$$\delta \alpha_{j} = \begin{cases} \delta \alpha \\ \delta \lambda \\ \delta e_{x} \\ \delta e_{y} \\ \delta i_{x} \\ \delta i_{y} \end{cases} = \begin{cases} (a_{j} - a_{c})/a_{c} \\ \lambda_{j} - \lambda_{c} + (\Omega_{j} - \Omega_{c})\cos i_{c} \\ e_{x_{j}} - e_{x_{c}} \\ e_{y_{j}} - e_{y_{c}} \\ i_{j} - i_{c} \\ (\Omega_{j} - \Omega_{c})\sin i_{c} \end{cases}$$
(1)

A common way to include in the dynamical description the effect of the differential atmospheric drag is to employ an augmented state vector, including the drifts in the relative semi-major axis and relative eccentricity vector due to the differential drag [32, 33]:

$$\delta\alpha_{j}^{*} = \{\delta\alpha_{j}, \delta\dot{a}_{drag}, \delta\dot{e}_{drag}, \delta\dot{\omega}_{drag}\}$$
 (2)

From this representation, the linearized dynamic, including the control term for the j-th satellite of the formation, is expressed in a state space formulation as:

$$\delta \dot{\alpha}_j^* = \mathbf{A}^{J_2, dd}(t, t_0) \delta \alpha_j^*(t) + \mathbf{B}(t) \mathbf{u}(t)$$
(3)

where the matrix  $\mathbf{A}^{J_2,dd}(t,t_0)$  includes the differential effects of the Keplerian motion, the differential Earth's oblateness, and the differential atmospheric drag; the matrix  $\mathbf{B}(t)$  is the control matrix, and the vector  $\mathbf{u}(t)$  is the control input in the relative Hill frame.

**Keplerian Contribution.** The unperturbed contribution in the matrix  $\mathbf{A}^{J_2,dd}(t,t_0)$  from Keplerian motion is based on the Hill-Clohessy-Wiltshire equations and can be expressed as [34, 35]:

$$\mathbf{A}^{hcw}(t,t_0) = \begin{bmatrix} 0 & \mathbf{0}_{2\times 5} \\ -1.5nt & \mathbf{0}_{4\times 1} & \mathbf{0}_{4\times 5} \end{bmatrix}$$
(4)

where the quantity  $\mathbf{0}_{l\times m}$  is a matrix full of zeros with dimensions  $\{l,m\}$ , t is the time variable, and n is the mean motion of the primary orbit  $n = \sqrt{\mu/a}$ , where  $\mu$  is the standard gravitational parameter for the Earth (approximately  $398600.4418 \cdot 10^{14} \, km^3/s^2$ ).

**Differential Earth Oblateness Contribution.** For a more accurate description of the relative dynamics in the LEO region, the first-order secular effect of the Earth's oblateness  $J_2$  is incorporated in the plant matrix of the system. Specifically, as demonstrated in the literature [36], it causes secular drift in the right ascension of the ascending node  $\dot{\Omega}$ , the argument of perigee  $\dot{\omega}$ , and the mean anomaly  $\dot{M}$  depending on the orbital inclination i and eccentricity e:

$$\begin{cases}
\dot{\Omega} \\
\dot{\omega} \\
\dot{M}
\end{cases} = \kappa_{J_2} \begin{cases}
-2\cos i \\
5\cos^2 i - 1 \\
\eta \left(3\cos^2 i - 1\right)
\end{cases}$$
(5)

where the parameter  $\kappa_{J_2} = \frac{3J_2R_\oplus^2\sqrt{\mu}}{4a^{7/2}\eta^4}$  includes the effect of the Earth's oblateness and the parameter  $\eta = \sqrt{1-e^2}$  retains the contribution of the eccentricity. To compute the plant matrix, we must differentiate Eq. 1 with respect to time and substitute in it the drift rates of Eq. 5, retaining the first-order Taylor expansion. Following a similar approach to the derivation in [32], it is possible to obtain a sparse plant matrix in a simple way, taking advantage of a linear rotation of the quasi-non-singular state  $\delta\alpha_j$ , based on a rotation of the eccentricity vector:

$$\delta \alpha_{i,mod} = \mathbf{J}_{mod} \delta \alpha_i \tag{6}$$

$$\mathbf{J}_{mod}(el_c) = \begin{bmatrix} \mathbf{I}^{2\times2} & \mathbf{0}^{2\times2} & \mathbf{0}^{2\times2} \\ \mathbf{0}^{2\times2} & \cos\omega & \sin\omega \\ -\sin\omega & \cos\omega \end{bmatrix}$$
(7)

This approach allows the decoupling of the effects of changes in eccentricity and argument of perigee on the relative eccentricity vector [32]. The resulting plant matrix  $\mathbf{A}_{mod}^{J2}$  will have a sparse behavior, and its expression was derived in

[32] for the following system:

$$\delta \dot{\alpha}_{j,mod} = \mathbf{A}_{mod}^{J2} \delta \alpha_{j,mod} \tag{8}$$

$$\mathbf{A}_{mod}^{J_{2}}(el_{c}) = \kappa_{J_{2}} \begin{bmatrix} 0 & 0 & 0 & 0 & 0 & 0 \\ -\frac{7}{2}EP & 0 & eFGP & 0 & -FS & 0 \\ 0 & 0 & 0 & 0 & 0 & 0 \\ -\frac{7}{2}eQ & 0 & 4e^{2}GQ & 0 & -5eS & 0 \\ 0 & 0 & 0 & 0 & 0 & 0 \\ -\frac{7}{2}S & 0 & -4eGS & 0 & 2T & 0 \end{bmatrix}$$
(9)

$$E = 1 + \eta F = 4 + 3\eta G = 1/\eta^{2}$$

$$P = 3 \cos^{2} i - 1 Q = 5 \cos^{2} i - 1 R = \cos i$$

$$S = \sin(2i) T = \sin^{2} i W = \cos^{2}(i/2)$$
(10)

Starting from the expression in Eq. 8, we have derived the expression of the plant matrix for the original state system with the quasi-non-singular state  $\delta \alpha_j$ . Substituting the expression of  $\delta \dot{\alpha}_{j,mod}$  from Eq. 6 in the state system of Eq. 8, we get the following expression:

$$\delta \dot{\alpha}_{j} = \mathbf{J}_{mod}^{-1} \left( \mathbf{A}_{mod}^{J_{2}} \mathbf{J}_{mod} - \dot{\mathbf{J}}_{mod} \right) \delta \alpha_{j} = \mathbf{A}^{J_{2}} \delta \alpha_{j}$$
(11)

where  $\mathbf{J}_{mod}^{-1}$  is the inverse matrix of  $\mathbf{J}_{mod}$ , and  $\dot{\mathbf{J}}_{mod}$  is the time derivative of  $\mathbf{J}_{mod}$ . Implementing the transformation, we recover the full expression for the plant matrix  $\mathbf{A}^{J_2}$  in Eq. 12. We can observe that  $\mathbf{A}^{J_2}$  has a similar structure to the one in Eq. 9, with an additional contribution due to the argument of perigee and its drift rate. The presented model is valid for quasi-circular orbits and small separations in eccentricity and argument of perigee.

$$\mathbf{A}^{J_{2}}(el_{c},\dot{e}l_{c}) = \kappa_{J_{2}} \begin{bmatrix} 0 & 0 & 0 & 0 & 0 & 0 \\ -\frac{7}{2}EP & 0 & e_{x}FGP & e_{y}FGP & -FS & 0 \\ \frac{7}{2}e_{y}Q & 0 & 4e_{x}e_{y}GQ + \sin\omega\dot{\omega} & -4e_{x}^{2}GQ - (1-\cos\omega)\dot{\omega} & 5e_{y}S & 0 \\ -\frac{7}{2}e_{x}Q & 0 & 4e_{x}^{2}GQ + (1-\cos\omega)\dot{\omega} & 4e_{x}e_{y}GQ - \sin\omega\dot{\omega} & -5e_{x}S & 0 \\ 0 & 0 & 0 & 0 & 0 & 0 \\ -\frac{7}{2}S & 0 & -4e_{x}GS & -4e_{y}GS & 2T & 0 \end{bmatrix}$$
(12)

Differential Atmospheric Drag Contribution. The inclusion of the differential drag is fundamental to modeling the dynamics in the LEO region. In the case of eccentric orbits, the main effect is the decay of the apogee radius over time while the perigee remains constant. On the other hand, when the eccentricity of the orbit tends to zero, as in the case of quasi-circular orbits, the effect of the atmospheric drag becomes significant on the perigee height, which starts to decrease. An approach for modeling the impact on near-circular orbits is the so-called density-model-free formulation, introduced in [32, 33]. The main effects caused by the atmospheric drag are secular drifts in the semi-major axis and eccentricity, as well as changes in true anomalies and arguments of perigee. The augmented quasi-non-singular ROEs state in Eq. 2 adequately captures these contributions. Starting from the work of [32, 33], we model the plant matrix to include the density-model-free formulation of the differential drag in the system dynamics:

$$\mathbf{A}^{dd}(el_c) = \begin{bmatrix} 1 & 0 & 0 \\ -\left(\frac{3}{2}n + \frac{7}{2}\kappa_{J_2}EP\right) & \kappa_{J_2}eFGP & 0 \\ 1 & 2\cos\omega - 4\kappa_{J_2}e^2GQ & -2\sin\omega \\ -\frac{7}{2}\kappa_{J_2}eQ & 2\sin\omega + 4\kappa_{J_2}e^2GQ & 2\cos\omega \\ 0 & 0 & 0 \\ \frac{7}{2}\kappa_{J_2}S & -4\kappa_{J_2}eGS & 0 \\ \mathbf{0}^{3\times6} & \mathbf{0}^{3\times3} \end{bmatrix}$$
(13)

**Overall System Dynamics.** From the preceding analysis, we can obtain the system dynamics, including the external perturbation contribution of the differential  $J_2$  and the differential drag:

$$\mathbf{A}^{J_2,dd}(el_c,\dot{el}_c) = \begin{bmatrix} \mathbf{A}^{hcw} + \mathbf{A}^{J_2} & \mathbf{A}^{dd} \\ \mathbf{0}^{3\times6} & \mathbf{I}^{3\times3} \end{bmatrix}$$
(14)

**Control Accelerations.** The control matrix  $\mathbf{B}(t)$  was derived to map the control accelerations  $\mathbf{u}(t)$  from the Hill reference frame to the ROE framework. The expression of the matrix  $\mathbf{B}(t)$  is derived in Eq. 15, where  $\theta$  is the true anomaly, and the parameter  $\chi = 1 + e_c \cos \theta$ . The complete derivation of the control matrix can be found in [37]. Note that the last three rows have been added to have a dimension consistent with the augmented state vector and must be

removed for the cases when only the  $J_2$  perturbation or the unperturbed relative motion is considered.

$$\mathbf{B}(t) = \frac{1}{a_c n_c \chi} \begin{bmatrix} \frac{2\chi}{\eta} e_c \sin \theta & \frac{2\chi}{\eta} (1 + e_c \cos \theta) & 0 \\ -2\eta^2 & 0 & 0 \\ \eta \chi \sin u_c & \eta \left( (2 + e_c \cos \theta) \cos u_c + e_x \right) & \frac{\eta e_y}{\tan i_c} \sin u_c \\ -\eta \chi \cos u_c & \eta \left( (2 + e_c \cos \theta) \sin u_c + e_y \right) & -\frac{\eta e_x}{\tan i_c} \sin u_c \\ 0 & 0 & \eta \cos u_c \\ 0 & 0 & \eta \sin u_c \\ 0 & 0 & 0 \\ 0 & 0 & 0 \end{bmatrix}$$
(15)

# III. Methodology

This section describes the motion planning strategy to design the reconfiguration between the fixed-baseline and the safe mode configurations. First, the optimal guidance is computed as the reference trajectory for the closed-loop dynamics. A convex optimization is implemented for this purpose, and the fuel-optimal trajectory to reconfigure the formation from the SAR phase to the safe mode is computed. Subsequently, three different algorithms are developed for the motion planning strategy. The proposed MPC in a closed loop is based on a reference guidance trajectory obtained with convex optimization. Then, the classical LQR is implemented based on a trial-and-error selection of the gain matrices. Finally, a novel adaptive LQR (aLQR) is proposed, implementing different heuristic algorithms to select the control gain automatically.

#### A. Reference Trajectory: Sequential Convex Optimization

The reference guidance trajectory is computed via a sequential convex optimization based on the linearization and discretization of the cost function, the system dynamics, and system constraints. In particular, we follow the derivation of the control problem based on the convexification of each term, similar to the approach in [14, 15, 17]. The maneuver is modeled with a constrained optimization problem to compute the control law and the trajectory to move a satellite from an initial position to a final position in a specific time interval, considering the constraints on the thrust level available and the collision avoidance among the satellites in the formation. To generate the guidance optimal trajectory, we considered the system under an unperturbed relative dynamic, excluding the effects of external perturbations.

First, the decision vector for the optimal system definition is derived to include the relative states (in terms of ROEs)

and the control vectors for each satellite in the formation. Assuming a multi-satellite system with j = 1, ..., N (with N the number of satellites), the decision vector  $\hat{\mathbf{X}}$  is defined in Eq. 16, where the couple  $(\delta \alpha_j, \mathbf{u}_j)$  contains the relative state  $\{\delta a, \delta \lambda, \delta e_x, \delta e_y, \delta i_x, \delta i_y\}_j$  and the control vector  $\{u_x, u_y, u_z\}_j$  of satellite j for each time step k. The chief can be included in the decision vector, for a decentralized control approach. In this case, the central or reference point of the formation becomes a virtual point, while the chief has the authority to maneuver with the same degrees of freedom as the deputies. Such can be beneficial for a situation where one of the deputies has a failure of the engine, and all the other satellites in the formation are required to perform an evasive maneuver, including the chief satellite. Considering a total of K time steps, the decision vector of each j-th satellite has dimensions 9K + 3(K - 1).

$$\hat{\mathbf{X}} = \{ \delta \alpha_1, \mathbf{u}_1, ..., \delta \alpha_i, \mathbf{u}_i, ... \delta \alpha_N, \mathbf{u}_N \}$$
(16)

The optimization aims to compute the trajectory with the minimum propellant consumption for the reconfiguration between the fixed-baseline and the safe mode configuration of the formation. Consequently, the cost function is defined by the sum of all the contributions to the control vector during the maneuver, and it can be expressed as in Eq. 17, where the index k represents the discretized time step k = 1, ..., K, where each time step is  $\Delta t$ . This discretization is applied thanks to the piecewise constant property of the control in each time step, and the norm-1 is used for an optimal solution with minimum fuel consumption.

$$\mathbf{J} = \sum_{k=1}^{K} \|\mathbf{u}_j[k]\|_1 \Delta t \tag{17}$$

Note that the type of norm used in the cost function depends on the thruster architecture. This study considers the satellites to have thrusters in each direction (radial, transversal, and normal) with a single fuel tank. In the case under analysis, the fuel is assumed to come from the same tank for each thruster, and norm-1 can be used to minimize the sum of the magnitude of the control components. Consequently, the strategy is equivalent to minimizing the total fuel used during the formation reconfiguration. On the other hand, for different configurations, the norm-2 or the norm- $\infty$  can be considered to describe the cost function adequately. For example, for a spacecraft with a single thruster, the norm-2 is better used to minimize the magnitude of the control components [26]. The cost function must be manipulated into a convex formulation in terms of the decision vector  $\hat{\mathbf{X}}$ . This procedure requires the definition of a matrix  $\mathbf{H}_j$  to extract the control terms  $\mathbf{u}_j[k]$  from the state vector of each j-th satellite, with  $\mathbf{x}_j$  identifying the couple  $(\delta \alpha_j, \mathbf{u}_j)$  for every j = 1, ..., N [15]:

$$\mathbf{H}_{j}\mathbf{x}_{j} = \left\{ \mathbf{0}_{1\times 6K}, \quad \mathbf{u}_{j}^{1}, \quad ..., \quad \mathbf{u}_{j}^{k}, \quad ..., \quad \mathbf{u}_{j}^{K-1} \right\}$$
 (18)

Finally, for the overall formation, the objective function is defined to include the contribution of each satellite, where  $\triangle t$  identifies the discrete time step:

$$\hat{\mathbf{J}} = \|(\hat{\mathbf{H}}\hat{\mathbf{X}})\Delta t\|_{1} \tag{19}$$

Note that the expression in Eq. 19 is equivalent to the objective function defined for the classical control problem in Eq. 17, as it corresponds to the sum of the norm-1 at each time instant k of the control effort  $\mathbf{u}_i[k]$ .

After defining the cost function, we identify the scenario's constraints. The first constraint that was considered is the relative dynamic under forced motion. The optimization is set up to derive the optimal reconfiguration trajectory under the selected dynamical model. Consequently, the relation in Eq. 3 is discretized at time step k, considering exclusively the contribution of the HCW in the state transition matrix of the relative dynamics:

$$\delta \alpha_j[k+1] = \left(\mathbf{I} + \mathbf{A}^{hcw}[k]dt\right)\delta \alpha_j[k] + \mathbf{B}[k] \Delta t \mathbf{u}_j[k]$$
(20)

Subsequently, the discretized system in Eq. 20 is manipulated to obtain a convex formulation of the constraint. First, the expression in 20 can be rewritten in matrix form for each *j*-th satellite.

$$\begin{bmatrix} \mathbf{0}_{6\times 6(k-1)}, & -\left(\mathbf{I}_{6}+\mathbf{A}^{hcw}\Delta t\right), & \mathbf{I}_{6}, & \mathbf{0}_{6\times 3(2K-k-3)}, & -\mathbf{B}\Delta t, & \mathbf{0}_{6\times 3(K-k-1)} \end{bmatrix} \cdot \mathbf{X}_{j} = \mathbf{A}_{sd} \cdot \mathbf{X}_{j} = \mathbf{0}, \quad (21)$$

where  $\mathbf{X}_j$  is the vector including the discretized state vector  $\delta \alpha_j[k]$  and the control vector  $\mathbf{u}_j[k]$ , for each step k. Finally, the overall system was obtained via the definition of a system dynamics matrix  $\hat{\mathbf{A}}_{sd}$  and the decision vector  $\hat{\mathbf{X}}$  as [15]. The former term includes the contribution of the discretized state transition matrix and the control matrix at each time step, and multiplies the couple  $(\delta \alpha_j, \mathbf{u}_j)$  at each time step:

$$\begin{bmatrix} \dots & \dots & \dots \\ \mathbf{0}_{6(K-1)\times M(j-1)} & \mathbf{A}_{sd} & \mathbf{0}_{6(K-1)\times M(N-1)} \\ \dots & \dots & \dots \end{bmatrix} \hat{\mathbf{X}} = 0$$
 (22)

$$\hat{\mathbf{A}}_{sd}\hat{\mathbf{X}} = 0 \tag{23}$$

where the parameter M is equal to 6K + 3(K - 1) Similarly, we impose the constraints on the initial and final conditions on the relative state of the formation following the procedure in [15]. The initial and final relative states of the formation are described by  $\delta \alpha_{j,0}$  and  $\delta \alpha_{j,0}$ , respectively.

$$\delta\alpha[k=1] = \delta\alpha_{j,0} \qquad \delta\alpha[k=K] = \delta\alpha_{j,f}. \tag{24}$$

As for the discretized relative dynamics, the expression in Eq. 24 can be expressed in convex formulation as  $\mathbf{A}_0 \hat{\mathbf{X}} = \mathbf{X}_0$ , and  $\mathbf{A}_f \hat{\mathbf{X}} = \mathbf{X}_f$ , where  $\mathbf{A}_0$  and  $\mathbf{A}_f$  are the matrices to extract the initial and final states at each time step k, and  $\mathbf{X}_0$  and  $\mathbf{X}_f$  are column vectors for the initial and final conditions of the overall formation. Then, we considered the limitation on

the control acceleration that the thruster can provide which is connected to the technological limitation of the onboard engine, and it is expressed as:

$$\|\mathbf{u}_j[k]\|_q \le \mathbf{u}_{max_j}.\tag{25}$$

To properly set a limit on the thrust level of each thruster, the norm- $\infty$  with  $q = \infty$  is used for the problem description. The matrix  $\mathbf{L}[k]$  is introduced to retrieve the inter-satellite relative distance from the ROE state of satellite i and satellite j at each time instant k. Finally, the constraint for collision avoidance among the satellites in the formation is paramount to ensure a safe reconfiguration. Its formulation was derived following the procedure identified in previous work [16], where the relative Cartesian position was expressed as a function of the ROEs. For a mapping between the ROE  $(\delta \alpha_j)$  and the relative Cartesian representation  $(\mathbf{x}_j)$ , a matrix  $\mathbf{L}$  is introduced to obtain the relative Cartesian position. A first-order mapping has been considered for the definition of the matrix  $\mathbf{L}$ :

$$\mathbf{x}_{j}[t] = \begin{bmatrix} a & 0 & -a\cos nt & -a\sin nt & 0 & 0\\ 0 & a & 2a\sin nt & -2a\cos nt & 0 & 0\\ 0 & 0 & 0 & a\sin nt & -a\cos nt \end{bmatrix} \boldsymbol{\delta}\alpha_{j}[t]$$
 (26)

The matrix  $\mathbf{L}$  is used to extract the relative Cartesian position from the ROEs space, and the safety distance constraint can be formulated for each couple i, j of satellites as:

$$|\mathbf{L}_{j}\delta\alpha_{j} - \mathbf{L}_{i}\delta\alpha_{i}|_{2} \ge d_{coll},$$
 (27)

where  $d_{coll}$  refers to the minimum inter-satellite distance accepted during the formation reconfiguration. Note that the chief satellite must be included in the definition of the couple i, j for the collision avoidance. Subsequently, the matrix  $\mathbf{L}$  is discretized in terms of time step k, and it is used to express the constraint for collision avoidance in a convex formulation, making use of an approximation with affine constraint [16, 26]:

$$\left(\mathbf{L}[k]\boldsymbol{\delta}\alpha_{j}[k] - \mathbf{L}[k]\boldsymbol{\delta}\alpha_{i}[k]\right)^{T}\left(\mathbf{L}[k]\boldsymbol{\delta}\alpha_{j}[k] - \mathbf{L}[k]\boldsymbol{\delta}\alpha_{i}[k]\right) \ge d_{coll}\|\mathbf{L}[k]\boldsymbol{\delta}\bar{\alpha}_{j}[k] - \mathbf{L}[k]\boldsymbol{\delta}\bar{\alpha}_{i}[k]\|_{2}$$
(28)

where  $\delta \bar{\alpha}_j$  and  $\delta \bar{\alpha}_i$  refer to the optimal solution found at the preceding iteration. The term  $d_{coll}$  accounts for the minimum inter-satellite distance during the maneuver and must include information on the dimensions of the satellites. The left side of the equation represents the scalar product of the current relative trajectory between the couple of satellites i, j and the trajectory at the preceding step. The right side of the inequality represents the norm-2 relative vector at the preceding step multiplied by the minimum inter-satellite distance. This is equivalent to asking the norm-2 of the current relative trajectory to be bigger than the minimum inter-satellite distance, giving again the expression

in Eq.27. This approach was proposed by [26] and used again in the approach developed in [16]. The value of  $d_{coll}$  was selected equal to the sum of the spacecraft diameter (assuming a sphere for the platform) and the prohibited zone for safety purposes. The convexification of the collision avoidance constraint results in a mapping of the forbidden zone from a spherical area centered around the satellite to a polygonal volume with each face perpendicular to the relative position vectors between each satellite of the formation [16, 26]. Because the constraint on the inter-satellite collision avoidance is based on the knowledge of the predicted trajectory evolution ( $\delta \bar{\alpha}_j$  and  $\delta \bar{\alpha}_i$ ), the solution of the open-loop optimal control at the very first step requires additional considerations, as the predicted trajectory is not yet available. For the initialization of the procedure, the optimal solution is computed without including the collision avoidance constraint. Then, this solution is used as input for a second iteration to obtain an optimal trajectory that is compliant with the collision avoidance constraint.

Once the control system has been defined, the solution of the open-loop optimal control is computed following the procedure in Algorithm 1, which implements a disciplined convex programming algorithm [38]. The notation used in the algorithm follows the formulation of the CVXPY Python-embedded modeling language for convex optimization problems [38–40]. The optimal guidance problem is defined and solved with the open-source, available algorithms in Python (i.e., CLARABEL or MOSEK [40]).

# Algorithm 1 Optimal guidance algorithm via sequential convex programming (CVX).

- 1: Input:
- 2: Number of Spacecraft N;
- 3: Chief's orbital elements  $el_c$ ;
- 4: Initial and Final State of each Satellite  $\delta \alpha_{i,0}$  and  $\delta \alpha_{i,f}$ ;
- 5: Maximum Thruster Acceleration **u**<sub>maxi</sub>;
- 6: Minimum Inter-Satellite Distance for Safe Flight  $d_{coll}$

#### 7: Initialization:

- 8: Initialize number of temporal steps *K* and the time step  $\Delta t = t^{k+1} t^k$
- 9: Initialize the auxiliary variable m = 6K + 3(K 1)
- 10: Initialize the decision vector  $\hat{\mathbf{X}}_{Nm\times 1}$

### 11: Routine for the CVX:

- 12: Define the Objective Function  $\hat{\mathbf{J}}$
- 13: Define the Constraints from Eq. 20, Eq. 24, Eq. 25, Eq. 28
- 14: Optimal Convex Problem = cp.Problem(Objective,Constraints)

#### 15: Solve with CLARABEL or MOSEK:

16: Return  $\hat{\mathbf{X}}_{opt}$  – optimal trajectory solution with  $(\delta \alpha_j, \mathbf{u_j})_{opt}$  for each satellite

#### **B. Model Predictive Control Design**

The first closed-loop control strategy for motion planning is based on the MPC feedback controller. Similar to previous works [24–27], the control objective is formulated as linear and quadratic expressions starting from Algorithm 1

to follow and correct the reference trajectory in the presence of external orbital perturbations. The control actions fed to the control system consist of a specific subset of the optimal control problem's global solution. The MPC minimizes a cost function via a numerical optimization algorithm and can be used to compute the corresponding control action via the discretization of the problem within a time interval (or time horizon). One common approach for the definition of the time interval at each time step is the receding horizon scheme that generates a fixed-size time window at each time step, always starting at the current sampling time (thus shifting during the simulation) [16, 41]. However, this approach is not suitable for our problem, as it does not allow direct control of the reconfiguration time. The reconfiguration design into the safe mode requires a short maneuver time (ideally less than one orbital period), which is typically pre-defined before reconfiguring the formation. Consequently, the approach based on the so-called shrinking horizon scheme has been adopted in the present manuscript. The shrinking horizon scheme is based on the definition of the final time instant, and the reconfiguration time interval is computed at each step, starting from the current to the final (fixed) time. This approach produces a time interval that reduces in time, as shown in Fig. 3. It is important to consider that this second approach could lead to higher computational costs or inaccuracies for cases requiring a long transfer time compared with the receding horizon. In the current work, the MPC is implemented as a feedback algorithm that accounts for mismatches and inaccuracies between the current states and the reference trajectory due to external disturbances not included in the analytical model for the reference trajectory generation. Specifically, at each step, the reference trajectory is computed as the solution of Algorithm 1, and the commanded control is implemented in the following step. The control logic is illustrated in Fig. 4. Differently for the reference trajectory computation of Section III.A, the relative dynamics is propagated, including the external perturbation modeled in Section III.A, i.e., the differential mean Earth's oblateness and the differential atmospheric drag. In the subsequent steps, the initial time is updated with the current time, defining the new horizon for each iteration. The algorithm computes the reference trajectory  $\delta \alpha^k$  and control action  $\mathbf{u}^k$  for each time instant k (with k=1,...,K) until the spacecraft reaches the desired position at the final time. The process is shown in more detail in Algorithm 2. This way of proceeding improves the stability of the optimal maneuver and the inclusion in the relative dynamic model of uncertainties and additional external perturbations (e.g., navigation uncertainties and high-fidelity orbital perturbations).

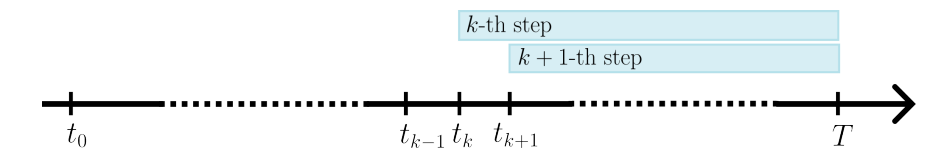


Fig. 3 Shrinking horizon scheme for the MPC.

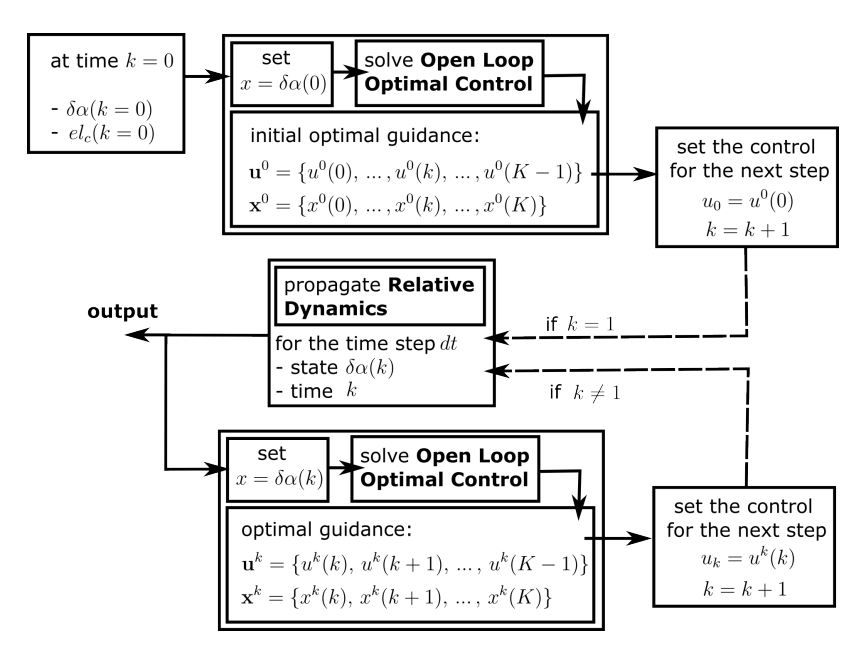


Fig. 4 Flow diagram for the MPC illustrating the adopted control logic.

# Algorithm 2 Closed-loop control algorithm via MPC.

- 1: Initialization:
- 2: solve Algorithm 1 for the optimal guidance  $\hat{\mathbf{X}}_{opt}$
- 3: set the reconfiguration time T
- 4: set  $k_0 = 0$

#### 5: Routine for the MPC:

- 6: while  $k_0 \le T$  do
- 7: set the time interval with  $k = k_0, ..., T$
- 8: solve Algorithm 1
- 9: get the optimal  $\hat{\mathbf{X}}_k$  at the current time with  $(\delta \alpha_j, \mathbf{u}_j)_{k,opt}$  of each satellite for  $k = k_0, ..., T$
- 10: Propagate the relative dynamics, including external disturbances (Eq. 14)
- 11: update  $(\delta \alpha_j, \mathbf{u}_j)_{k,opt}$  to the current trajectory
- 12: update  $k_0$  to the current time
- 13: end while
- 14: **Output:**
- 15: retrieve  $(\delta \alpha_j, \mathbf{u}_j)_k$  from the relative dynamic propagation
- 16: assess the control error of the actual  $\delta lpha_j$  w.r.t. the optimal guidance

#### C. Classical Linear Quadratic Controller

The second approach for the design of the closed-loop control law investigated in the current manuscript is based on the linear quadratic regulator (LQR). The LQR is one of the most used and tested methods for optimal feedback control. Starting from the representation of the system dynamics as a state space expression, as in Equation (3), we define the desired final state to achieve as  $\delta \alpha_i |_{d}(t)$ , and the error between the desired state and the actual state equal to:

$$\mathbf{x}_{err}(t) = \delta \alpha_i(t) - \delta \alpha_i|_d(t) \tag{29}$$

Then, the objective function to track a desired state can be defined as a quadratic performance function:

$$J_{lqr} = \frac{1}{2} \int_{t_0}^{t_f} \left( \mathbf{x}_{err}^T \mathbf{Q} \mathbf{x}_{err} + \mathbf{u}^T \mathbf{R} \mathbf{u} \right) dt$$
 (30)

where  $\mathbf{Q}$  is the weight matrix of the error in the optimization process between the current and the desired state, and it is a positive definite matrix;  $\mathbf{R}$  is the weight matrix of the control variables in the optimization process, and it is a semi-definite matrix. From Eq. 30, the minimization of the cost function is obtained by solving the Riccati equation for the optimal control law of the system:

$$\mathbf{P}\mathbf{A} + \mathbf{A}^T \mathbf{P} - \mathbf{P} \mathbf{B} \mathbf{R}^{-1} \mathbf{B}^T \mathbf{P} + \mathbf{Q} = -\dot{\mathbf{P}}$$
(31)

For the case under analysis in the current manuscript, we considered no time dependence on the Riccati equation, solving the minimization of the cost function via the algebraic version of Eq. 31 with  $\dot{\mathbf{P}} = 0$ . The corresponding feedback control is computed from the solution of Eq. 31 as:

$$\mathbf{u}(t) = -\mathbf{R}^{-1}\mathbf{B}^{T}\mathbf{P}\mathbf{x}_{err}(t)$$
(32)

where the matrix  $\mathbf{R}^{-1}\mathbf{B}^T\mathbf{P}$  is the control gain. Note that in the definition of the cost function and the Riccati equation, we have considered the spacecraft dynamics, including only the effect of the differential mean Earth's oblateness. In contrast, the differential drag contribution is considered exclusively in the propagation of the feedback loop. To solve the Riccati Equation, we need to know the dynamic and control system matrices,  $\mathbf{A}^{J_2,dd}$  and  $\mathbf{B}$  (see the derivation in Section II), and the weight matrices  $\mathbf{Q}$  and  $\mathbf{R}$ , that have the following expression:

$$\mathbf{Q} = \operatorname{diag}\left(q_{x}, q_{y}, q_{z}, q_{v_{x}}, q_{v_{y}}, q_{v_{z}}\right)$$

$$\mathbf{R} = \operatorname{diag}\left(r_{x}, r_{y}, r_{z}\right)$$
(33)

corresponding to a total of 9 variables to set up the LQR. Most past studies relied on a trial-and-error approach to determine these decision variables [42, 43], although some studies proposed entry values for specific problem geometries. For example, in [44], the control weights for a projected circular orbit formation were selected from the mean motion of the reference orbit: the control weights in  $\mathbf{R}$  were chosen equal to  $1/n^4$ , and the state weights in  $\mathbf{Q}$  equal to  $n^{-2}$ , with n the mean motion of the orbit. However, to enhance the stability and flexibility of the LQR control to different formation configurations, we propose an approach to determine the decision variables of the weight matrices based on evolutionary algorithms and presented hereafter.

# D. Optimal Linear Quadratic Controller via Evolutionary Algorithms

Only a few studies exist that optimize the tuning of the weighting matrices  $\mathbf{Q}$  and  $\mathbf{R}$  via evolutionary algorithms. The work in [45] proposes a tuning strategy of the LQR to design an autopilot for an aircraft roll control system. Its analysis tested the performance of three algorithms: the genetic algorithm (GA), the particle swarm optimization (PSO), and the artificial bee colony (ABC). Similarly, the work in [46] proposes an automatic tuning of the LQR based on an entropy search of Bayesian optimization for the case of a humanoid robot. However, existing studies have not been applied to spacecraft formation flying control in the direction of optimal tuning of the LQR weighting matrices. The current work proposes a novel procedure to automatically select the control gains independently from the formation geometry. The optimization is set up to get the best weights of matrices  $\mathbf{Q}$  and  $\mathbf{R}$  while minimizing the propellant consumption. We identify the following fitness functions that minimize control usage and the time integral of the LQR tracking error  $\mathbf{x}_{err}(t)$ :

$$f_1(x) = \int_0^T |\mathbf{u}_j(t)|_1 dt; \qquad f_2(x) = \int_0^T t |\mathbf{x}_{err}(t)|_2 dt$$
 (34)

The function in  $f_2(x)$  is called the integral time absolute error (ITAE), and it is commonly used in combination with LQR control problems [47]. Eq. 34 defines a multi-objective optimization [48]:

$$\min F(x) = [f_1(x), f_2(x)]$$

$$s.t., \begin{cases} \text{inequality constraints} & g_m(x) \le 0 \\ \text{equality constraints} & h_p(x) = 0 \end{cases}$$
(35)

where the indices m and p represent the number of equality and inequality constraints, respectively. The constraints for this problem have been derived similarly to those in Algorithm 1, as we want to constrain the maximum control thrust and the collision avoidance among the spacecraft in the formation. Additionally, we included in the constraint the bounds on the maximum and minimum value for the parameters of matrices  $\mathbf{Q}$  and  $\mathbf{R}$ , to reduce the exploration interval. These bounds were selected by running a reduced number of simulations with manual tuning to identify the appropriate interval for the optimization. Multi-objective optimization can be approached with strategies such

as Pareto-front optimality or penalty functions definition [48–50]. However, for our trajectory tracking applications, the position error between the actual trajectory and the desired one must be kept below a certain threshold, leading to the definition of a constraint instead of a direct optimization of  $f_2(x)$ . Consequently, we reduced the problem to a single-objective constraint optimization in the direction of reducing the complexity of the problem and improving the simulation performance. The problem in Eq. 35 is modified into the following single-objective constrained optimization:

$$\min F(x) = [f_1(x)]$$
additional constraint  $f_2(x) \le \varepsilon$ 

$$\text{inequality constraint} \quad g_j(x) \le 0$$

$$\text{equality constraint} \quad h_i(x) = 0$$
(36)

where the ITAE function has been included in the problem as an additional constraint, and  $\varepsilon$  represents the threshold value of the ITAE. Specifically, the integral time absolute error must respect the threshold  $\varepsilon$ , derived from the maximum tracking error acceptable for the configuration under analysis. The problem defined in Eq. 36 is easier to solve than the multi-objective optimization, but at the same time, it correctly considers the constraint on the ITAE. The optimization procedure was set up considering the components of matrices  $\mathbf{Q}$  and  $\mathbf{R}$ . The initial population x from Eq 33:

$$\mathbf{x} = [q_x, q_y, q_z, q_{v_x}, q_{v_y}, q_{v_z}, r_x, r_y, r_z]$$
(37)

leading to a 9-dimensional decision vector for the optimization. Because the high dimensionality of the problem results in a worsening of the performance from a solving time point of view, we have also investigated the case of 2, 3, and 5 decision variables and compared the results in terms of optimal fitness function and processing time. Three reduced decision vectors were identified equal to:

$$\mathbf{x}' = [q_x', q_y', r_x, r_y, r_z]$$

$$\mathbf{x}'' = [q_x'', q_y'', r'']$$

$$\mathbf{x}''' = [q''', r''']$$

where the weights for the matrix  $\mathbf{Q}$  have been considered the same for the position components  $q'_x$  and  $q''_x$ , and velocity components  $q'_v$  and  $q''_v$  in both x' and x'', respectively. Additionally, the same weights for matrix  $\mathbf{R}$  have been considered r'' in x''. For the decision vector x''', only one gain is associated with matrices  $\mathbf{Q}$  and  $\mathbf{R}$ , respectively.

After defining the cost function and the decision vectors, a novel approach was derived for single-objective constraint

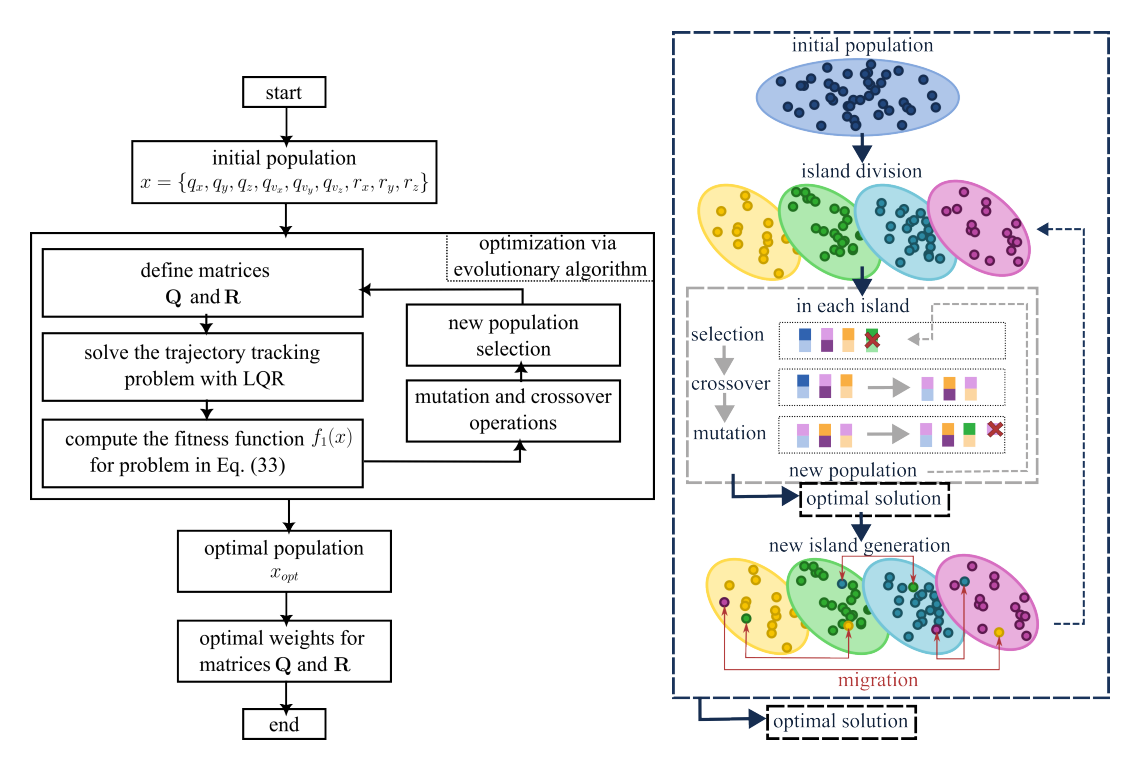
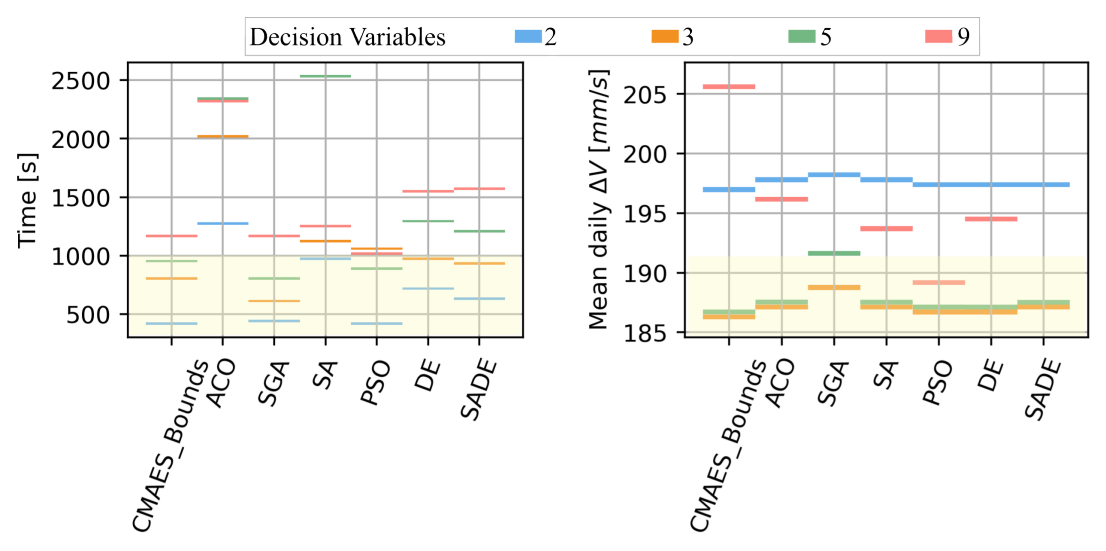


Fig. 5 Flow chart for weight optimization via evolutionary algorithms (left) and schematic illustration of selection, crossover, and mutation within each island from the initial population (right).

optimization via evolutionary algorithms. From the definition of the initial population x, we iteratively solve the trajectory tracking problem of Eq 31, and we compute the fitness function of the system in Eq 36. At each iteration, the initial population undergoes a mutation and crossover operation to define the new population for improving the fitness function  $f_1(x)$ . At the end of the procedure, we obtain the optimal decision vector, containing the weights for the matrices **Q** and **R**, that minimize the fitness function  $f_1(x)$  and at the same time respect the constraints of Eq 36. This procedure is represented as a flow chart in Fig. 5 (left). The optimization procedure is implemented via the library in Python Parallel Global Multi-objective Optimizer (PyGMO), developed by the European Space Agency [51]. This tool is especially powerful for solving constrained, unconstrained, single-objective, and multi-objective optimizations, and it already provides several heuristic algorithms that can be used to optimize a problem via their evolutionary method. Some examples of the available algorithms are Differential Evolution (DE), Particle Swarm Optimization (PSO), Artificial Bee Colony (ABC), Simple Genetic Algorithm (SGA), or the Covariance Matrix Adaptation-ES [51]. During the optimization setup, we considered an initial population of  $N_p$  with a given number of generations of  $N_p$ , after which no fitness improvement occurred. Additionally, to divide the original population into substructures, we have considered the island model to improve population diversity [52, 53]. This way, the initial population is divided into multiple islands  $(N_i)$  where selection, crossover, and mutation operations are performed to obtain the best individuals for the fitness function. The best individuals identify the new islands, where migration of individuals is performed to



- ACO: Extended Ant Colony Optimization
- SADE: Self-Adaptive Differential Evolution
- DE: Differential Evolution
- PSO: Particle Swarm Optimization
- SGA: Simple Genetic Algorithm
- SA: Simulated Annealing
- CMAES\_Bounds: Covariance Matrix Adaptation Evolution Strategy with Bounds

Fig. 6 Performance of the optimization procedure for automatic tuning of the LQR controller: processing time (left) and delta-velocity budget (right).

increase diversity and improve the global search for the next generation. The procedure is repeated until there is no improvement in the fitness function or the maximum number of generations is reached. The flowchart of this procedure is depicted in Fig. 5 (right). The performance of the optimization procedure was tested against the orbit maintenance of a Helix trajectory (see the parameters  $a\delta\alpha_{i,f}$  in Table 1) to assess the best decision vector among  $\mathbf{x}, \mathbf{x}', \mathbf{x}'', \mathbf{x}'''$ . Considering the single-objective constraint optimization in Eq. 36, we compute the mean daily delta-velocity budget for maintaining the helix trajectory under external orbital perturbations and the computational time for solving the problem with multiple available optimization algorithms. The results are depicted in Fig. 6, where four different colors have been used to represent each decision vector case. The light-yellow squares indicate the area with the best performance from both the convergence time and cost function point of view. As expected, we observe that for most optimization algorithms, the cases with only two or three decision variables (i.e.,  $\mathbf{x}'', \mathbf{x}'''$ ) are more efficient from a computational point of view, up to a reduction of factor 2: the higher the number of decision variables, the higher computational time. In contrast, for the Simulated Annealing, a different behavior was observed, as the five decision variable cases resulted in a higher convergence time than the case with nine variables. This was due to a convergence issue for the case with five variables, and it was observed only with this specific optimization algorithm. A second important consideration comes from the delta-v budget, which directly indicates the cost function. The results show that all the optimization algorithms converge to the optimal solution for the different decision vectors. However, for the case of 5 and 9 decision variables, the convergence time is higher, indicating issues during the convergence. Looking at the best performance

in terms of the minimum objective function, i.e., minimum delta velocity, we identify how the cases with 3 and 5 decision variables perform better for most algorithms. Additionally, from the delta-velocity point of view, the Particle Swarm Optimization (PSO) performs well for 3, 5, and 9 decision variables. At the same time, the Covariance Matrix Adaptation Evolution Strategy with Bounds (CMAES Bound) ensures the lowest mean daily delta velocity. In most of the cases, the best computational time is achieved for the case of 3 decision variables, i.e.,  $\mathbf{x}''$ , with an improvement in the convergence time of more than 50%, and with a similar delta-v budget performance to the case of 5 decision variables. Additionally, as a result of the analysis, reducing the number of decision variables did not impact the accuracy of the solution, leading to similar results from the formation reconfiguration trajectory point of view. Consequently, as the only difference results from the computational time and the accuracy, one of the three approach can be selected with no loss of generality in the subsequent analysis. Going in the direction of improving the computational time while keeping comparable performance, the case of 3 decision variables, with  $\mathbf{x}'' = [q_x'', q_y'', r'']$ , has been considered in Section IV, for the automatic gain selection of the aLQR approach.

#### IV. Simulations

Starting from the problem setting in Section II and the methodology in Section III, this section presents the simulation results to perform a maneuver to the safe mode configuration under the different control strategies presented in Section III. The simulation aims to design a reconfiguration maneuver in less than one orbital period to change the formation configuration from the fixed-baseline acquisition phase to the safe mode (see Fig. 2).

#### A. Parameters and boundary conditions

The initial and final configurations for the scenario under analysis are depicted in Fig. 2. The corresponding parameters and boundary conditions for the simulation are reported in Table 1. The initial conditions correspond to the formation geometry under a fixed-baseline configuration, with the chief at the center and two deputies with a baseline

Table 1 Simulation parameters and boundary conditions.

Parameter	Symbol	Unit of Measure	Value	
Initial Conditions	$a\delta lpha_{j,0}$	m	$j = 1  \{0, 0, 0, 0, 4, -40\}$ $j = 2  \{0, 0, 0, 0, -4, 20\}$	
Final Conditions	$a\deltalpha_{j,f}$	m	$j = 2  \{0, 0, 0, 0, 3, -4, 20\}$ $j = 1  \{0, 0, 0.5, -60, 0.5, -60\}$ $j = 2  \{0, 0, -0.5, 30, -0.5, 30\}$	
Chief Absolute Orbit	$\mathbf{el}_c$	(km,-,-,deg,deg,deg)	$\{7153, 8e - 5, 5e - 5, 98.5, 30, 0\}$	
Maneuver Time	$T_f$	seconds	0.8 orbital period	
Safety Distance	$d_{coll}$	m	6	
Spacecraft Mass	$m_{sc}$	kg	500	
Maximum Control Acceleration	$ \mathbf{u}_{max} $	$\mathrm{ms}^{-2}$	3e - 5	
Maximum Relative Position Error	arepsilon	m	0.1	

purely in the across-track direction of the Hill reference frame, with no separation in radial or along-track directions. The final condition after the maneuver is selected to respect the (anti-) parallel condition of relative eccentricity and inclination vectors for passive safety, resulting in the well-known Helix relative trajectory [11]. The maneuver time was selected below one orbital period to ensure a fast reconfiguration to the safe mode, but it could be relaxed depending on the actual operational constraints.

An important consideration must be made regarding the maximum relative position error considered in Table 1. Achieving a maximum relative position error of 0.1 m is challenging and requires precise orbit navigation and robust control methodologies. The methodologies proposed in this study, the MPC and the LQR, offer the advantage of adaptability and optimal stability. Specifically, the MPC based on ROEs allows the trajectory to be planned and the control inputs to be adjusted based on future state predictions. This improves the formation behavior under external disturbances [11]. In contrast, the LQR is a widely used control method, which ensures the system's stability, refining the control effort via the minimization of the cost function [54]. The use of robust control methodologies must be coupled with the current advancements in the relative navigation techniques. Most of LEO missions are based on GNSS navigation, and formation flying configurations take advantage of the carrier-phase differential GNSS techniques such as real-time-kinematics (RTK) or precise pointing position (PPP) [55, 56]. Additionally, multi-sensor fusion employing Extended and Unscented Kalman Filters (EKF/UKF) contributes to real-time state estimation, integrating GNSS, IMU, and vision-based data [57]. A recent example of precise relative navigation and onboard autonomy under closed-loop control is ESA's mission PROBA-3, launched in 2024 [58, 59].

#### B. Guidance Trajectory: Fixed-Baseline Acquisition to Safe Mode

The first step is the generation of the guidance trajectory via the sequential convex optimization procedure of Algorithm 1. We perform the design by considering a discretization of 500 steps in the time frame of the reconfiguration. During the simulation, we observed that the CLARABEL solver provides better stability and performance in the algorithm convergence for the configuration under analysis. For this reason, we perform both the guidance design and the MPC algorithm with this solver. Fig. 7 (left) shows the optimal guidance trajectory in time, where the initial and final formation geometries are propagated for two orbital periods, and the optimal guidance is depicted with a bold segment. A gray line represents the trajectory of the chief at the center of the formation. We can observe how, in the initial leg, the across-track position is kept constant to guarantee fixed baselines for SAR interferometry [9].

The optimal maneuver reconfigures the deputies into two nested helix relative trajectories, propagated for two orbital periods after the maneuver. Looking then at the time evolution of the x and y components of the relative eccentricity and inclination vector, the maneuver imposes a change to set a parallel relative eccentricity and inclination vectors  $\delta e/\delta i$  for both deputies, as shown in Fig. 7 (right). Multiple works demonstrated that this condition ensures a passively safe relative motion [11–13]. Finally, the commanded thrust profile during the maneuver is shown in Fig. 8. Considering the

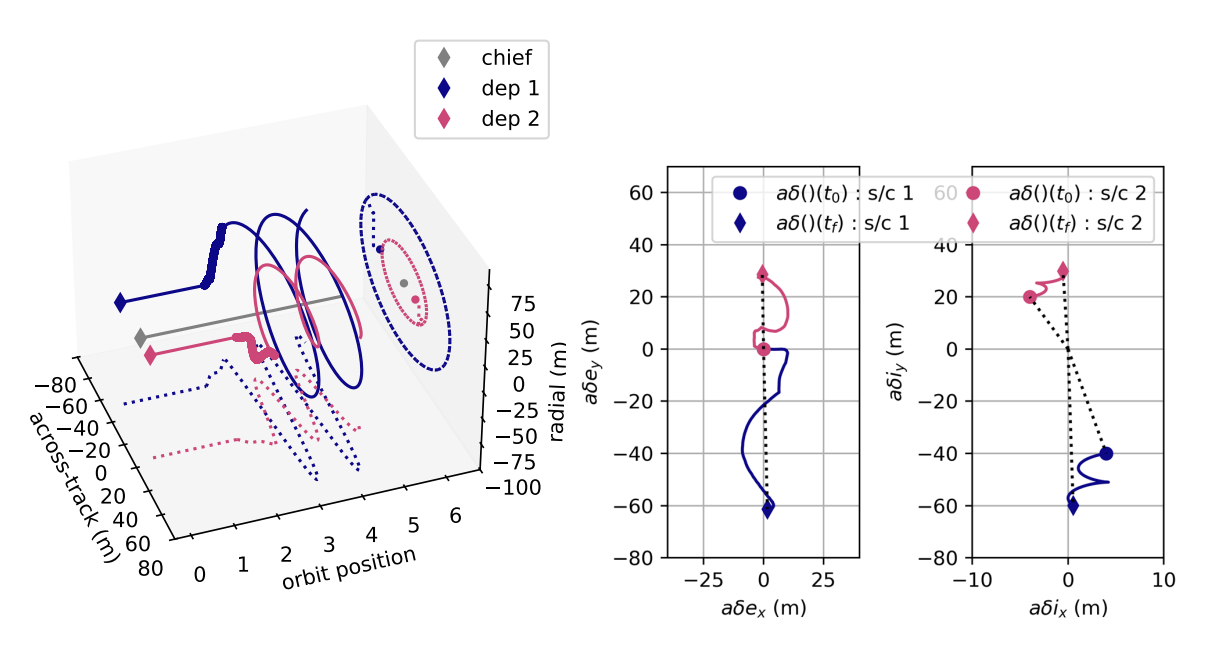


Fig. 7 Optimal guidance trajectory via sequential convex programming of Algorithm1: the three-dimensional representation in the Hill frame (left), and the evolution of  $\delta e/\delta i$  vectors (right).

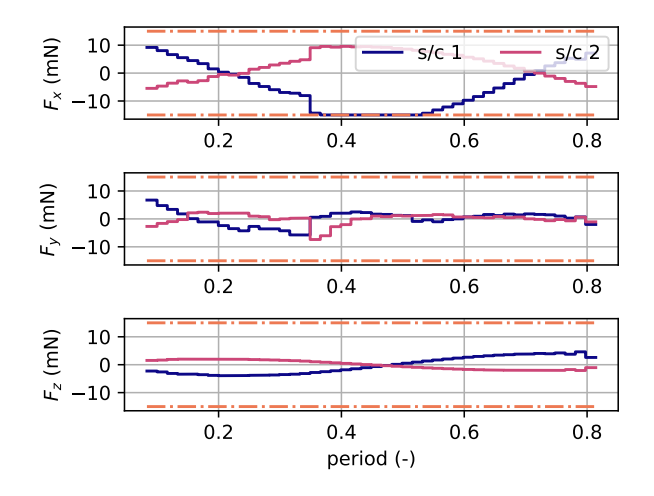


Fig. 8 Commanded thrust profile for the optimal guidance trajectory.

condition in Table 1, the maximum thrust level for the maneuver is equal to 15 mN, represented by the dashdot line in the graph. The reconfiguration is possible considering such limitation for deputies 1 and 2, assuming full engine capabilities on board. Similarly, the feasibility of the thrust profile in case of engine failure is also investigated in Section IV.E, as in [28].

# C. Trajectory Tracking with Model Predictive Control

The first maneuver planning approach is based on the MPC in Algorithm 2. Specifically, we design a maneuver to reconfigure the formation following the optimal guidance for the transition between the fixed-baseline acquisition

and the safe mode, as shown in Fig. 7. In the dynamical model of the MPC, we have included the full perturbation model derived in Section II, with Earth's oblateness and atmospheric drag. Additionally, the final time for the shrinking horizon scheme was equal to  $T_f$  of Table 1. To further test the stability of the solution, we have performed a simulation in a Monte Carlo fashion, considering 100 initial conditions in proximity to the fixed-baseline acquisition geometry, described by  $a\delta\alpha_{i,0}$ , including an error to simulate the navigation reconstruction uncertainties. A random distribution of the 100 samples has been considered, with a mean value equal to the  $a\delta\alpha_{i,0}$  parameter in Table 1, and a standard deviation of 50 cm for the relative mean argument of latitude and 10 cm for the remaining ROEs components. The number of time steps K at each run of the MPC was set equal to 100 to reduce the computational burden of the solution and, at the same time, maintain good accuracy in the maneuver design. The parameters for the setup of the MPC are summarized in 2. Fig. 9(left) shows the evolution of the relative eccentricity and inclination vectors  $\delta e/\delta i$  during the reconfiguration with the MPC algorithm. We can observe that all the trajectories reconfigure correctly to the target condition  $a\delta\alpha_{i,f}$ , ensuring anti-parallel condition for the passive safety. Comparing it to the results in Fig. 7(right), it is evident how the evolution of the relative eccentricity vector is more affected by the initial uncertainties during the MPC simulation, whereas for the relative inclination angle, all the conditions follow very similar trajectories. Similarly, Fig. 9(right) depicts the error in the ROEs components during the maneuver. The error has been computed as the difference between the current condition at the step k and the target parameters  $a\delta\alpha_{i,f}$ . Fig. 9(right) shows how the

Table 2 Parameters for the setup of the MPC for trajectory tracking.

Parameter	Value
Monte Carlo samples	100
Number of time steps	100
Standard deviation on $a\delta a_j$ and $a\delta \lambda_j$	50 cm
Standard deviation on $a\delta e_x$ , $a\delta e_y$ , $a\delta i_x$ , $a\delta i_y$	10 cm

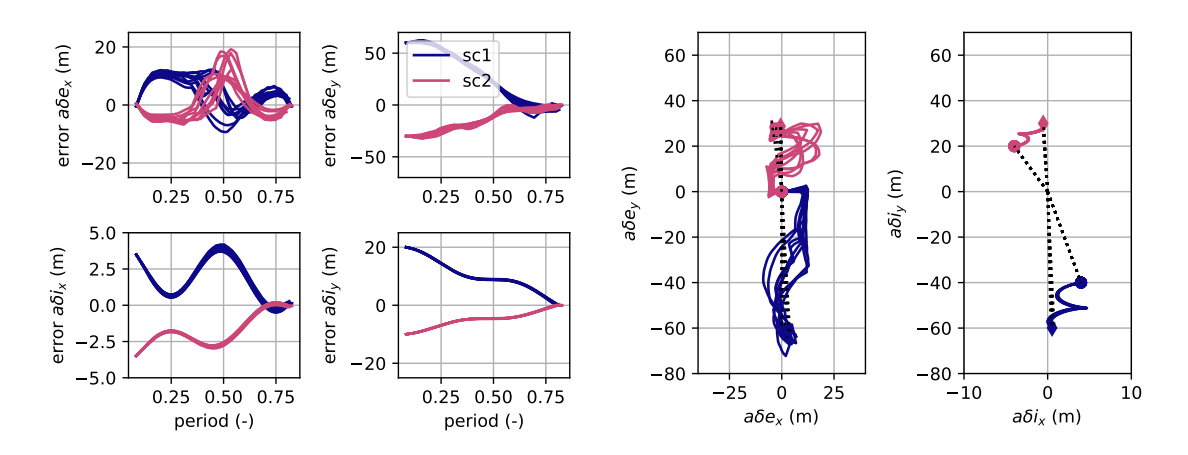


Fig. 9 Reconfiguration maneuver via MPC: error between the current and the target state  $a\delta\alpha_{j,f}$  (left) and components of the relative  $\delta e/\delta i$  vectors (right).

ROEs correctly reconfigure to the final configuration for all 100 initial conditions under analysis.

## D. Trajectory Tracking with the Adaptive Linear Quadratic Regulator

In this section, we evaluate the performance of the aLQR to follow a reference trajectory. We compared the results with the manually tuned LQR and the MPC methodologies. Specifically, we have implemented and tested four approaches: the case of MPC, the classical LQR with manual tuning, the adaptive aLQR with full control capabilities, and the adaptive aLQR without radial control (setting  $u_x = 0$ ).

For the automatic tuning of the aLQR controller, we follow the procedure described in Fig. 5. Table 3 shows the selected parameters for the optimization procedure via evolutionary algorithms. We choose a population size of 25 individuals, divided into 5 islands, and run the optimization for 50 generations. These values were determined after a trade-off analysis between convergence performance and computational time. We then computed the optimal gain values for the weight matrices  $\bf Q$  and  $\bf R$ . Table 4 presents the optimal gains for the weight matrices  $\bf Q$  and  $\bf R$ , obtained by solving the problem in Fig. 5 for the scenario in Table 1. As detailed in Section III, the optimal parameters were determined for the case of three decision variables  $\bf x''=[q_x,q_v,r]$ . Furthermore, Table 4 shows that only minor adjustments of the parameters are necessary for the case where  $u_x=0$ , while the orders of magnitude remain consistent. Conversely, for the classical LQR cases, the gain matrix parameters were derived starting from literature values for manual tuning with slight adjustments (see Section III). The weight matrices were used to implement the LQR to track the optimal guidance trajectory of Fig. 7. Like the MPC approach, the closed-loop dynamics incorporate the main perturbations of the LEO region. The main difference between the two methods is that the LQR cannot adapt to anomalous conditions different from the predefined ones or automatically plan for a new optimal trajectory. In fact, the LQR relies on reference trajectories precomputed using additional algorithms.

Figure 10 presents the convergence profiles for the reconfiguration maneuver of deputy no. 1 under different control strategies. Specifically, the MPC approach yields a smoother and more stable trajectory, characterized by the absence of overshoots and reduced oscillations. This improved stability derives from the receding horizon framework, in which the

Table 3 Parameters for the heuristic optimization for automatic tuning of the LQR controller.

Parameter	Symbol	Value
Population	$N_p$	25
Islands	$N_i$	5
Generations	$N_g$	50

Table 4 Selected gain for the weight matrices Q and R for the LQR cases under analysis.

LQR Case	Matrix <b>Q</b>	Matrix <b>R</b>
aLQR	diag (8.66, 8.66, 8.66, 1.33, 1.33, 1.33) · 1 <i>e</i> 3	diag (1.94, 1.94, 1.94) · 1 <i>e</i> 11
aLQR $(u_x = 0)$	diag $(6.32, 6.32, 6.32, 4.76, 4.76, 4.76) \cdot 1e3$	diag (1.30, 1.30, 1.30) · 1e11

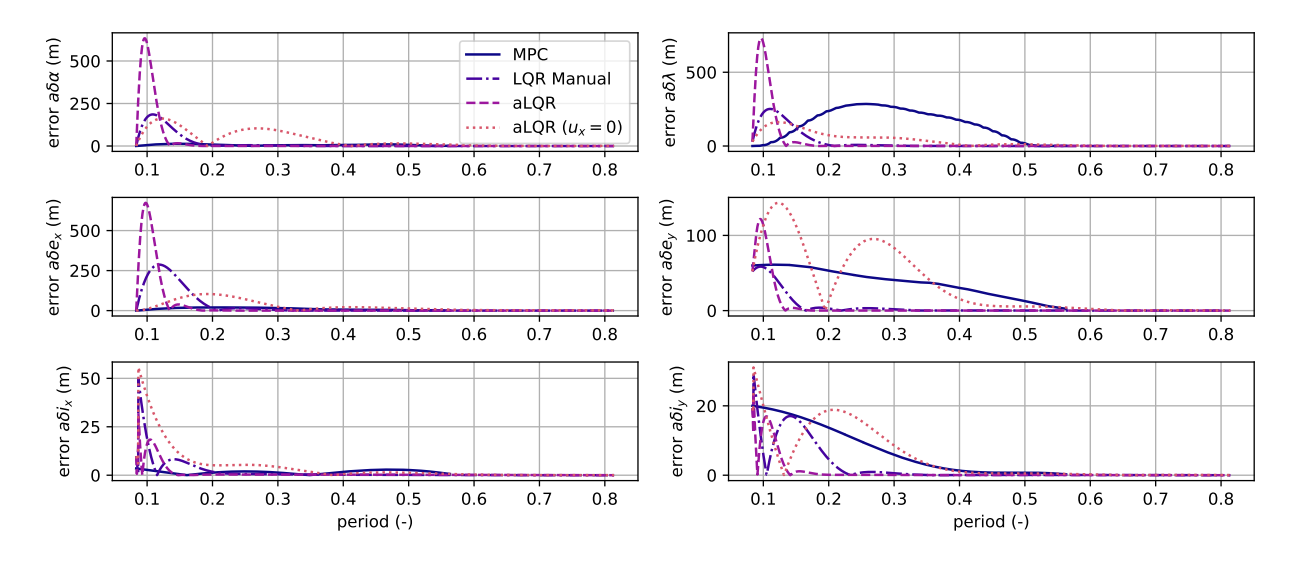


Fig. 10 Convergence profile for different algorithms to implement the reconfiguration between the fixed-baseline and safe modes for deputy no. 1.

optimal control sequence is continuously updated based on the evolving system state. However, this benefit comes at the cost of a longer convergence time, due to the conservative nature of MPC in satisfying constraints across the prediction horizon. In contrast, the LQR implementations demonstrate faster convergence rates, resulting in a rapid achievement of the final formation configuration. Nevertheless, this efficiency comes with greater sensitivity to dynamic perturbations, pronounced oscillations, and overshoot phenomena in the tracking error. Among the LQR implementations, the aLQR under full actuation shows the shortest convergence time. Conversely, reducing the control authority, by removing the radial thrust component, delays the convergence and amplifies transient instabilities.

Furthermore, we also evaluated performance metrics to compare the four approaches in Fig. 10. Table 5 presents the delta-velocity budget for the maneuver using different control methodologies for deputies 1 and 2. The most efficient algorithm for the case under analysis is the MPC, which shows delta-v values of approximately 12 mm/s and 7 mm/s. In contrast, the manually tuned LQR is the least efficient approach, as the controller gains were not optimized for the desired configuration. On the other hand, the aLQR results are comparable to those of the MPC, demonstrating the advantages of the automatic gain selection. As expected, removing the control effort in the radial direction leads to a slightly improved maneuver efficiency from a propellant consumption point of view [44]. Regarding the position error between the final state and the desired helix trajectory, both the MPC and the two versions of the aLQR guarantee a terminal position error below 10 cm, as indicated by the threshold  $\varepsilon$ . On the other hand, the manually tuned LQR exhibits the worst convergence profile, with a terminal error of up to 80 cm and 73 cm for the two deputies, respectively. Lastly, we assessed the algorithm's running time, running the simulations with an Intel<sup>®</sup> Core<sup>TM</sup> i7 processor at 1.90 GHz and 32 GB of RAM. The MPC performs better than the aLQR optimization procedure, requiring less computational effort. Specifically, the aLQR relies on heuristic algorithms that necessitate the definition of a large initial population for

Table 5 Performance figures for the formation reconfiguration using different control algorithms.

Control Methodology	Delta-v Budget		Terminal Position Error		Algorithm Running Time
	(mm/s)		(cm)		(minutes)
	deputy 1	deputy 2	deputy 1	deputy 2	
Model Predictive Control (MPC)	≈ 12	≈ 7	$\leq 10 (1\sigma)$	$\leq 10 (1\sigma)$	≈ 4
Classical LQR (manual tuning)	$\approx 22$	≈ 20	$\approx 80  (1\sigma)$	$\approx 73  (1\sigma)$	_
aLQR with full control capabilities	≈ 14	≈ 11	$\leq 10  (1\sigma)$	$\leq 10  (1\sigma)$	≈ 45
aLQR with $u_x = 0$	≈ 13	≈ 10	$\leq 10  (1\sigma)$	$\leq 10  (1\sigma)$	≈ 65

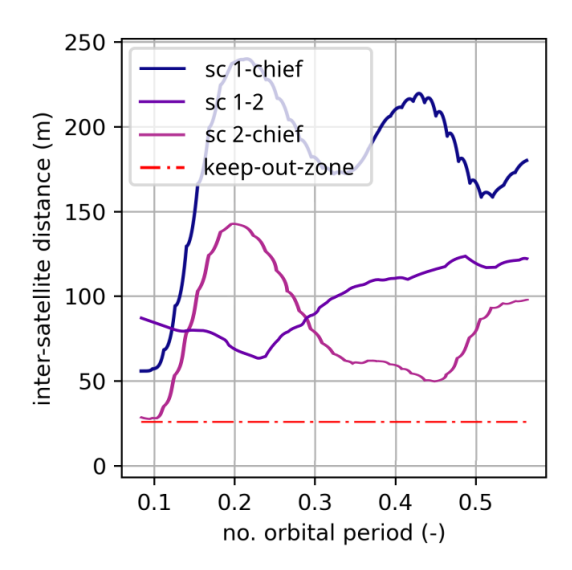


Fig. 11 Time evolution of the inter-satellite distance in time during the maneuver.

convergence. In contrast, classical manual tuning requires several trial-and-error iterations depending on the selected formation geometry, and its computational time was not assessed. In fact, the literature values provided in [44] are derived for the case of Projected Circular Orbit of the relative motion and require further tuning when the relative geometry is different. Finally, the time evolution of the distance among the satellites is reported in Figure 11. We can observe that the minimum threshold is respected throughout the maneuver, keeping the reconfiguration safe.

# E. Safe Mode Acquisition under Engine Failure with Model Predictive Control

The final scenario under analysis considers the same initial conditions and parameters of Table 1. Additionally, an engine failure for deputy no. 1 was considered, so it can no longer control its relative trajectory. Due to the nature of the fixed baseline configuration defined by the initial conditions, when one of the deputies loses controllability, its relative motion undergoes a natural oscillation in the across-track trajectory. This behavior generates a collision risk with the other satellites in the formation. The strategy adopted in this scenario is the following. As deputy no. 1 detects a failure of one of the engines and cannot control its trajectory, an alert message should be transmitted from deputy no 1 to the

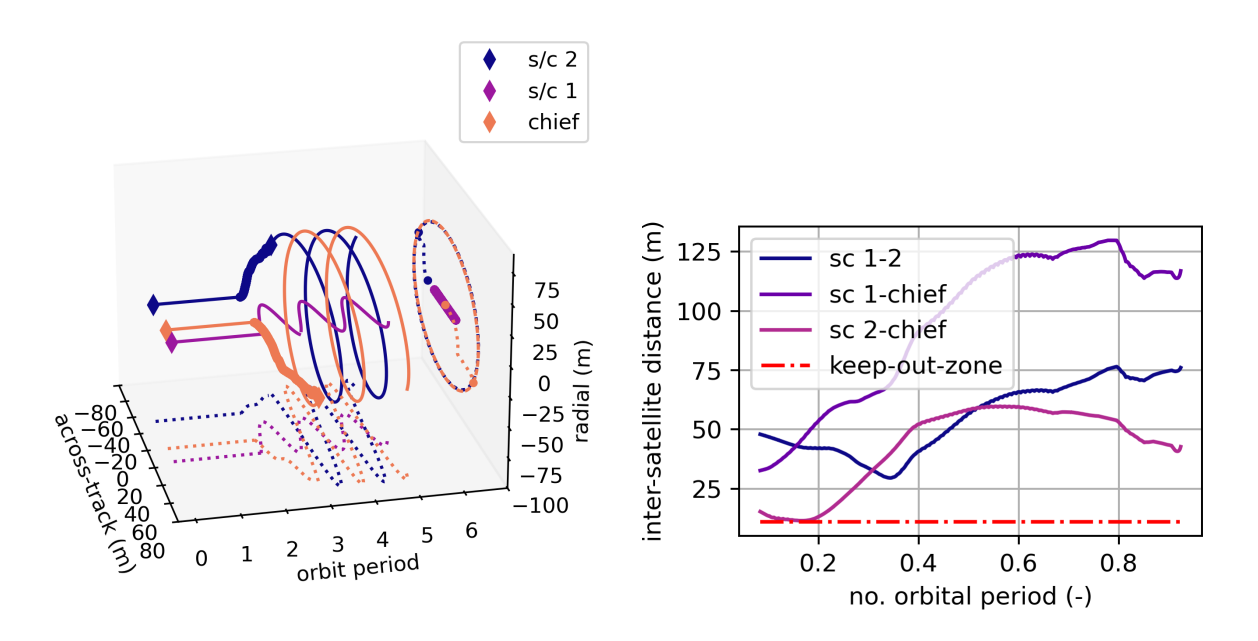


Fig. 12 Reconfiguration maneuver under the case of engine failure for deputy no. 1 (left), with inter-satellite distance evolution in time (right).

other satellites, the chief and the deputy no. 2, via an omnidirectional radio-frequency transmission. This approach triggers deputy no. 2 and the chief satellite to immediately implement a maneuver to move away and reconfigure to a helix geometry around deputy no. 1. In this scenario, it is of paramount importance to include all the satellites in the methodology formulation of the sequential convex programming and the MPC of Section III Additionally, during the reconfiguration maneuver, the deputy 2 and the chief account for the natural motion of the deputy 1, and the maneuver is designed by the MPC accordingly. To further enhance safety during the reconfiguration, the minimum inter-satellite distance was increased to 10 m, and it identifies a keep-out zone. Figure 12(left) represents the time evolution of the trajectory in the radial-transversal-normal plane for the case of engine failure of deputy no.1. Specifically, it illustrates an initial phase of 2 orbital periods where the formation keeps the fixed-baseline configuration. Then, deputy no 1 undergoes an engine failure and loses the capability to control its relative position, resulting in an oscillatory motion in the across-track direction. At that moment, the chief and the deputy no.2 begin the reconfiguration maneuver to move away from the deputy no. 1. The reconfiguration is performed in about one orbital period, and the intersatellite distance is monitored during the maneuver, as shown in Figure 12(right). It can be observed that the keep-out zone is respected for each couple of satellites in the formation, and that the maneuver gradually increases the inter-satellite distance. The delta-velocity for the maneuver was assessed as 22 mm/s and 18 mm/s, for the chief and the deputy satellite number 2, respectively. Finally, deputy no. 2 and the chief satellites are reconfigured in a helix relative trajectory around the fault satellite. Depending on the capability of the system to recover from the failure on deputy no.1, an additional reconfiguration manoeuvre might be designed to further move the satellites away from deputy no.1, for example, increasing the absolute orbit altitude and continuing the mission operation in a different orbital tube. With this approach, we demonstrate the additional flexibility of the MPC to deal with the failure of one of the satellites in the formation.

# V. Conclusion

This paper develops and analyses multiple control strategies for maneuver planning in multi-satellite formation flying. First, we propose a model predictive control algorithm in combination with sequential convex programming. This approach incorporates the challenges of predictive capabilities and fixed-time convergence while considering uncertainties and external perturbations. Then, we propose a novel adaptive linear quadratic regulator (aLQR) to improve the tracking performance for a specified guidance trajectory while ensuring that the maximum terminal position error remains within  $\pm 10cm$ . The proposed approaches demonstrated their capability to achieve fast convergence, even when a limitation on the maximum thrust level and a minimum distance limitation for collision avoidance are imposed. Both algorithms ensure convergence despite external disturbances, keeping the delta-velocity budget in the order of a few centimeters per second.

Additionally, the heuristic technique to automatically compute the optimal gains for the LQR shows promising results in addressing the guidance tracking problem, offering a solution to the trial-and-error method commonly used in traditional LQR design. However, the main limitations of the proposed aLQR lie in the complexity of the heuristic optimization for onboard implementation and the algorithm running time, which becomes even more critical when considering limited onboard computational capabilities. This aspect might limit the applicability of the aLQR for autonomous onboard control, and further validation through hardware-in-the-loop simulations is necessary to assess its relevance.

Overall, this study addresses the need for robust and rapid formation reconfiguration into a safe mode, contributing to efficient solutions toward mission autonomy. Additionally, it supports the formation architecture of multiple satellites that cannot rely on passive safety configurations due to payload constraints, such as the fixed-baseline application for enhancing future single-pass InSAR applications or space-based applications that require close proximity among the satellites under entirely forced relative motion.

# **Funding Sources**

This work was partially funded by the European Union (ERC Starting Grant Distributed Radar Interferometry and Tomography Using Clusters of Smallsats (DRITUCS) 101076275). Views and opinions expressed are, however, those of the authors only and do not necessarily reflect those of the European Union or the European Research Council Executive Agency. Neither the European Union nor the granting authority can be held responsible for them.

#### References

- [1] Massonnet, D., and Feigl, K. L., "Radar interferometry and its application to changes in the Earth's surface," *Reviews of Geophysics*, Vol. 36, No. 4, 1998, pp. 441–500. https://doi.org/10.1029/97RG03139.
- [2] Gill, E., and Runge, H., "Tight formation flying for an along-track SAR interferometer," *Acta Astronautica*, Vol. 55, No. 3, 2004, pp. 473–485. https://doi.org/10.1016/j.actaastro.2004.05.044.
- [3] Krieger, G., Hajnsek, I., Papathanassiou, K. P., Younis, M., and Moreira, A., "Interferometric Synthetic Aperture Radar (SAR) Missions Employing Formation Flying," *Proceedings of the IEEE*, Vol. 98, No. 5, 2010, pp. 816–843. https://doi.org/10.1109/JPROC.2009.2038948.
- [4] Moreira, A., Prats-Iraola, P., Younis, M., Krieger, G., Hajnsek, I., and Papathanassiou, K. P., "A tutorial on synthetic aperture radar," *IEEE Geoscience and Remote Sensing Magazine*, Vol. 1, No. 1, 2013, pp. 6–43. https://doi.org/10.1109/MGRS.2013.2248301.
- [5] Krieger, G., Moreira, A., Fiedler, H., Hajnsek, I., Werner, M., Younis, M., and Zink, M., "TanDEM-X: A Satellite Formation for High-Resolution SAR Interferometry," *IEEE Transactions on Geoscience and Remote Sensing*, Vol. 45, No. 11, 2007, pp. 3317–3341. https://doi.org/10.1109/TGRS.2007.900693.
- [6] Massonnet, D., "Capabilities and limitations of the interferometric cartwheel," *IEEE Transactions on Geoscience and Remote Sensing*, Vol. 39, No. 3, 2001, pp. 506–520. https://doi.org/10.1109/36.911109.
- [7] Moreira, A., Krieger, G., Hajnsek, I., Hounam, D., Werner, M., Riegger, S., and Settelmeyer, E., "TanDEM-X: a TerraSAR-X add-on satellite for single-pass SAR interferometry," *IGARSS 2004. 2004 IEEE International Geoscience and Remote Sensing Symposium*, Vol. 2, 2004, pp. 1000–1003 vol.2. https://doi.org/10.1109/IGARSS.2004.1368578.
- [8] Mittermayer, J., Krieger, G., Bojarski, A., Zonno, M., Villano, M., Pinheiro, M., Bachmann, M., Buckreuss, S., and Moreira, A., "MirrorSAR: An HRWS Add-On for Single-Pass Multi-Baseline SAR Interferometry," *IEEE Transactions on Geoscience and Remote Sensing*, Vol. 60, 2022, pp. 1–18. https://doi.org/10.1109/TGRS.2021.3132384.
- [9] Scala, F., Krieger, G., and Villano, M., "Investigation of Fixed Across-Track Baselines for Distributed Spaceborne SAR Systems," EUSAR 2024; 15th European Conference on Synthetic Aperture Radar, 2024, pp. 32–37. URL https://elib.dlr.de/204285/.
- [10] Scala, F., Krieger, G., and Villano, M., "Investigation of multiple-satellite formation configurations for single-pass synthetic aperture radar interferometry," 75th International Astronautical Congress (IAC), 14-18 October 2024, Milan, Italy, 2024, pp. 1–6. https://doi.org/10.52202/078362-0082.
- [11] D'Amico, S., and Montenbruck, O., "Proximity Operations of Formation-Flying Spacecraft Using an Eccentricity/Inclination Vector Separation," *Journal of Guidance, Control, and Dynamics*, Vol. 29, No. 3, 2006, pp. 554–563. https://doi.org/10.2514/1. 15114.
- [12] Scala, F., Peixoto, M. N., Krieger, G., and Villano, M., "On the Safety of Multiple Satellite Formations for Synthetic Aperture Radar Applications," *Journal of Guidance, Control, and Dynamics*, Vol. 48, No. 2, 2025, pp. 414–423. https://doi.org/10.2514/1.G008407.

- [13] Koenig, A. W., and D'Amico, S., "Robust and Safe N-Spacecraft Swarming in Perturbed Near-Circular Orbits," *Journal of Guidance, Control, and Dynamics*, Vol. 41, No. 8, 2018, pp. 1643–1662. https://doi.org/10.2514/1.G003249.
- [14] Sarno, S., Guo, J., D'Errico, M., and Gill, E., "A guidance approach to satellite formation reconfiguration based on convex optimization and genetic algorithms," *Advances in Space Research*, Vol. 65, No. 8, 2020, pp. 2003–2017. https://doi.org/10.1016/j.asr.2020.01.033.
- [15] Scala, F., Gaias, G., Colombo, C., and Martín-Neira, M., "Design of optimal low-thrust manoeuvres for remote sensing multi-satellite formation flying in low Earth orbit," *Advances in Space Research*, Vol. 68, No. 11, 2021, pp. 4359–4378. https://doi.org/10.1016/j.asr.2021.09.030.
- [16] Montero Miñan, A., Scala, F., and Colombo, C., "Manoeuvre planning algorithm for satellite formations using mean relative orbital elements," *Advances in Space Research*, Vol. 71, No. 1, 2023, pp. 585–603. https://doi.org/10.1016/j.asr.2022.09.043.
- [17] Belloni, E., Silvestrini, S., Prinetto, J., and Lavagna, M., "Relative and absolute on-board optimal formation acquisition and keeping for scientific activities in high-drag low-orbit environment," *Advances in Space Research*, Vol. 73, No. 11, 2024, pp. 5595–5613. https://doi.org/10.1016/j.asr.2023.07.051.
- [18] Wie, B., Space Vehicle Dynamics and Control, Second Edition, American Institute of Aeronautics and Astronautics, Inc., 2008. https://doi.org/10.2514/4.860119.
- [19] Bryson, A. E., and Ho, Y.-C., Applied Optimal Control, Hemisphere Publishing Corporation, Washington, D.C., 1975. ISBN: 9780470114810. https://doi.org/10.1201/9781315137667.
- [20] Starin, S., Yedavalli, R., and Sparks, A., "Design of a LQR controller of reduced inputs for multiple spacecraft formation flying," *Proceedings of the 2001 American Control Conference*. (Cat. No.01CH37148), Vol. 2, 2001, pp. 1327–1332 vol.2. https://doi.org/10.1109/ACC.2001.945908.
- [21] Starin, S. R., Yedavalli, R. K., and Sparks, A. G., "Spacecraft formation flying maneuvers using linear-quadratic regulation with no radial axis inputs," *AIAA Guidance, Navigation, and Control Conference and Exhibit, August 2001, Motreal, Canada*, 2001, p. 4029. https://doi.org/10.2514/6.2001-4029.
- [22] Rasheed, L. T., "Optimal Tuning of Linear Quadratic Regulator Controller Using Ant Colony Optimisation Algorithm for Position Control of a Permanent Magnet DC Motor," *Iraqi Journal of Computers, Communications, Control and System Engineering*, Vol. 20, No. 3, 2020, pp. 29–41. https://doi.org/10.33103/uot.ijccce.20.3.3.
- [23] Hassani, K., and Lee., W.-S., "Optimal tuning of linear quadratic regulators using quantum particle swarm optimization," *Proceedings of the International Conference on Control, Dynamic Systems, and Robotics (CDSR'14)*, 2014, p. 15. URL https://api.semanticscholar.org/CorpusID:18284120.
- [24] Eren, U., Prach, A., Koçer, B. B., Raković, S. V., Kayacan, E., and Açıkmeşe, B., "Model Predictive Control in Aerospace Systems: Current State and Opportunities," *Journal of Guidance, Control, and Dynamics*, Vol. 40, No. 7, 2017, pp. 1541–1566. https://doi.org/10.2514/1.G002507.

- [25] Acikmese, B., Scharf, D., Hadaegh, F., and Murray, E., "A Convex Guidance Algorithm for Formation Reconfiguration," AIAA Guidance, Navigation, and Control Conference and Exhibit, 21-24 August, Keystone, Colorado (USA), 2006, p. 6070. https://doi.org/10.2514/6.2006-6070.
- [26] Morgan, D., Chung, S.-J., and Hadaegh, F. Y., "Model Predictive Control of Swarms of Spacecraft Using Sequential Convex Programming," *Journal of Guidance, Control, and Dynamics*, Vol. 37, No. 6, 2014, pp. 1725–1740. https://doi.org/10.2514/1.G000218.
- [27] Weiss, A., Baldwin, M., Erwin, R. S., and Kolmanovsky, I., "Model Predictive Control for Spacecraft Rendezvous and Docking: Strategies for Handling Constraints and Case Studies," *IEEE Transactions on Control Systems Technology*, Vol. 23, No. 4, 2015, pp. 1638–1647. https://doi.org/10.1109/TCST.2014.2379639.
- [28] Scala, F., Krieger, G., and Villano, M., "Design of Safety Procedures for a Multi-Satellite Formation Using a Continuous Control Scheme," 2024 AAS/AIAA Astrodynamics Specialist Conference, Broomfield (CO), August 11-15, 2024. URL https://elib.dlr.de/204683/.
- [29] D'Amico, S., "Autonomous formation flying in low earth orbit," Ph.D. thesis, Doctoral dissertation, TU Delft, Delft, The Netherlands, 2010. URL https://elib.dlr.de/63481/.
- [30] Spiridonova, S., Kirschner, M., and Hugentobler, U., "Precise mean orbital elements determination for LEO monitoring and maintenance," 24th International Symposium on Space Flight Dynamics, 2014. URL https://elib.dlr.de/103814/1/Spiridonova\_ISSFD\_2014\_upd.pdf.
- [31] Gaias, G., Colombo, C., and Lara, M., "Analytical Framework for Precise Relative Motion in Low Earth Orbits," *Journal of Guidance, Control, and Dynamics*, Vol. 43, No. 5, 2020, pp. 915–927. https://doi.org/10.2514/1.G004716.
- [32] Koenig, A. W., Guffanti, T., and D'Amico, S., "New State Transition Matrices for Spacecraft Relative Motion in Perturbed Orbits," *Journal of Guidance, Control, and Dynamics*, Vol. 40, No. 7, 2017, pp. 1749–1768. https://doi.org/10.2514/1.G002409.
- [33] Gaias, G., Ardaens, J.-S., and Montenbruck, O., "Model of  $J_2$  perturbed satellite relative motion with time-varying differential drag," *Celestial Mechanics and Dynamical Astronomy*, Vol. 123, 2015, p. 411–433. https://doi.org/10.1007/s10569-015-9643-2.
- [34] Hill, G. W., "Researches in the lunar theory," *American journal of Mathematics*, Vol. 1, No. 1, 1878, pp. 5–26. https://doi.org/10.2307/2369430.
- [35] Clohessy, W. H., and Wiltshire, R. S., "Terminal Guidance System for Satellite Rendezvous," *Journal of the Aerospace Sciences*, Vol. 27, No. 9, 1960, pp. 653–658. https://doi.org/10.2514/8.8704.
- [36] Brouwer, D., "Solution of the problem of artificial satellite theory without drag," Astronomical Journal, Vol. 64, 1959, p. 378. https://doi.org/10.1086/107958.
- [37] Steindorf, L. M., D'Amico, S., Scharnagl, J., Kempf, F., and Schilling, K., "Constrained low-thrust satellite formation-flying using relative orbit elements," 27th AAS/AIAA Space Flight Mechanics Meeting, Vol. 160, 2017, pp. 3563–3583.

- URL https://www.researchgate.net/publication/332072543\_Constrained\_Low-Thrust\_Satellite\_Formation-Flying\_Using\_Relative\_Orbit\_Elements.
- [38] Boyd, S. P., and Vandenberghe, L., Convex optimization, Cambridge university press, 2004. ISBN: 9780521833783. https://doi.org/10.1017/CBO9780511804441.
- [39] Grant, M. C., and Boyd, S. P., "Graph Implementations for Nonsmooth Convex Programs," *Recent Advances in Learning and Control*, edited by V. D. Blondel, S. P. Boyd, and H. Kimura, Springer London, London, 2008, pp. 95–110. https://doi.org/10.1007/978-1-84800-155-8\_7.
- [40] Diamond, S., and Boyd, S., "CVXPY: A Python-Embedded Modeling Language for Convex Optimization," *Journal of Machine Learning Research*, Vol. 17, No. 83, 2016, pp. 1–5. URL http://jmlr.org/papers/v17/15-408.html.
- [41] Capannolo, A., Zanotti, G., Lavagna, M., and Cataldo, G., "Model predictive control for formation reconfiguration exploiting quasi-periodic tori in the cislunar environment," *Nonlinear Dynamics*, Vol. 111, No. 8, 2023, pp. 6941–6959. https://doi.org/10.1007/s11071-022-08214-8.
- [42] Ke, Z., Zhenqi, H., and Meibo, L., "Study on maintaining formations during satellite formation flying based on SDRE and LQR," *Open Physics*, Vol. 15, No. 1, 2017, pp. 394–399. https://doi.org/doi:10.1515/phys-2017-0043.
- [43] Guarnaccia, L., Bevilacqua, R., and Pastorelli, S. P., "Suboptimal LQR-based spacecraft full motion control: Theory and experimentation," *Acta Astronautica*, Vol. 122, 2016, pp. 114–136. https://doi.org/10.1016/j.actaastro.2016.01.016.
- [44] Vadali, S. R., Sengupta, P., Yan, H., and Alfriend, K. T., "Fundamental Frequencies of Satellite Relative Motion and Control of Formations," *Journal of Guidance, Control, and Dynamics*, Vol. 31, No. 5, 2008, pp. 1239–1248. https://doi.org/10.2514/1.34790.
- [45] Abdulla, A., Mohammed, I., and Jasim, A., "Roll control system design using auto tuning LQR technique," *International Journal of Engineering and Innovative Technology*, Vol. 6, No. 2, 2017, pp. 11–22. https://doi.org/10.17605/OSF.IO/CHFU2.
- [46] Marco, A., Hennig, P., Bohg, J., Schaal, S., and Trimpe, S., "Automatic LQR tuning based on Gaussian process global optimization," 2016 IEEE International Conference on Robotics and Automation (ICRA), 2016, pp. 270–277. https://doi.org/10.1109/ICRA.2016.7487144.
- [47] Deng, X., Sun, X., Liu, R., and Wei, W., "Optimal analysis of the weighted matrices in LQR based on the differential evolution algorithm," 2017 29th Chinese Control And Decision Conference (CCDC), 2017, pp. 832–836. https://doi.org/10.1109/CCDC. 2017.7978635.
- [48] Liang, J., Ban, X., Yu, K., Qu, B., Qiao, K., Yue, C., Chen, K., and Tan, K. C., "A Survey on Evolutionary Constrained Multiobjective Optimization," *IEEE Transactions on Evolutionary Computation*, Vol. 27, No. 2, 2023, pp. 201–221. https://doi.org/10.1109/TEVC.2022.3155533.

- [49] Bianchessi, N., Cordeau, J.-F., Desrosiers, J., Laporte, G., and Raymond, V., "A heuristic for the multi-satellite, multi-orbit and multi-user management of Earth observation satellites," *European Journal of Operational Research*, Vol. 177, No. 2, 2007, pp. 750–762. https://doi.org/10.1016/j.ejor.2005.12.026.
- [50] Hua, Y., Liu, Q., Hao, K., and Jin, Y., "A Survey of Evolutionary Algorithms for Multi-Objective Optimization Problems With Irregular Pareto Fronts," *IEEE/CAA Journal of Automatica Sinica*, Vol. 8, No. 2, 2021, pp. 303–318. https://doi.org/10.1109/ JAS.2021.1003817.
- [51] Biscani, F., Izzo, D., Jakob, W., Acciarini, G., Martens, M., and Mereta, A., "esa/pagmo2: pagmo 2.17.0 (v2.17.0)," Zenodo, 2017. https://doi.org/10.5281/zenodo.4585131.
- [52] Wang, C., Yu, S., Chen, W., and Sun, C., "Highly efficient light-trapping structure design inspired by natural evolution," *Scientific reports*, Vol. 3, No. 1, 2013, p. 1025. https://doi.org/10.1038/srep01025.
- [53] He, W., Tang, X., Ji, W., Meng, L., Wei, J., Cao, D., Ma, C., Li, Q., and Lin, C., "An improved multi-island genetic algorithm and its utilization in the optimal design of a micropositioning stage," *Expert Systems with Applications*, Vol. 257, 2024, p. 125029. https://doi.org/10.1016/j.eswa.2024.125029.
- [54] Yamanaka, K., and Ankersen, F., "New state description of relative motion for on-orbit formation flying," *AIAA Guidance, Navigation, and Control Conference*, 2002. https://doi.org/10.2514/6.2002-4531.
- [55] Montenbruck, O., and et al., "Precision orbit determination for LEO satellites using onboard GPS receivers," *GPS Solutions*, Vol. 19, No. 4, 2015, pp. 673–686. https://doi.org/10.1007/s10291-015-0458-5.
- [56] Li, X., and et al., "Real-time precise point positioning: A new approach for precise orbit determination," *GPS Solutions*, Vol. 24, 2020, p. 71. https://doi.org/10.1007/s10291-020-00977-x.
- [57] He, W., and et al., "Fixed-Time Adaptive Sliding Mode Control for Spacecraft Formation Flying with Bounded Disturbances," *Acta Astronautica*, Vol. 197, 2022, pp. 342–350. https://doi.org/10.1016/j.actaastro.2022.04.024.
- [58] Benn, M., Jørgensen, J. L., Timmerman, L., Jørgensen, P. S., Denver, T., Pedersen, D. A., Rougeot, R., and Serrano, D., "Intersatellite Synchronization Module for Optical Sync and Data between Formation Flying Spacecraft," 2024 IEEE Aerospace Conference, IEEE, 2024, pp. 1–8. URL https://orbit.dtu.dk/en/publications/intersatellite-synchronization-module-for-optical-sync-and-data-b.
- [59] Ramarao, G., and Raju, G., "Advances in Satellite Ranging Methods Towards Precise Orbit Determination." *Defence Science Journal*, Vol. 75, No. 2, 2025. URL https://publications.drdo.gov.in/ojs/index.php/dsj/issue/view/720.